Ocean Engineering 272 (2023) 113866

Contents lists available at ScienceDirect

Ocean Engineering

journal homepage: www.elsevier.com/locate/oceaneng

Hydrodynamics of morphology for thunniform swimmers: Effects of the posterior body shape

Shun Huang, Dilong Guo, Yiwei Wang, Guowei Yang, Bo Yin *

Key Laboratory for Mechanics in Fluid Solid Coupling Systems, Institute of Mechanics, Chinese Academy of Sciences, Beijing, 100190, China
School of Engineering Science, University of Chinese Academy of Sciences, Beijing, 100049, China

ARTICLE INFO

Keywords:
Morphology
Posterior body of tuna
Biological fluid dynamics
Immersed boundary method
Fluid–structure interaction

ABSTRACT

Morphology of posterior body for thunniform swimmers plays an important role in determining the propulsion performance. Recent literature mainly focused on the effects of thunniform swimmers specialized features, e.g., finlets, crescent caudal fin, etc. However, it is unknown to what extent posterior body morphological change is optimized for hydrodynamic performance. In this paper, by varying the height and width of posterior body, numerical simulations of thunniform swimming at cruising state have been carried out. To account for the influence of fluid–structure interaction on the hydrodynamic performance, a sharp-interface immersed boundary method (IBM) is utilized to solve the incompressible viscous flow. As the width or height increases, stronger PBV_s (posterior body vortices) are generated alongside the posterior body. Then the constructive interaction between PBV_s and LEV_s (vortex generated on the leading edge of caudal fin) could enhance the caudal fin thrust significantly. This thrust enhancement mechanism is more evident with increasing height of the posterior body. The pressure difference between two sides of posterior body resulting from PBV_s helps diminish the trunk drag, which is more evident as width is decreased. Subsequently, a systematic study of the Reynolds number (Re) and Strouhal number (St) effects has been conducted to quantify and evaluate the hydrodynamic performance with various posterior body shapes. Our work can help understand tuna fish propulsion mechanism due to posterior body morphology, based on which engineered bionic swimmers can reach excellent swimming performance by optimizing the trunk shape.

1. Introduction

Physico-mechanical designs evolved from fish and other aquatic animals are currently inspiring robotic devices for propulsion in underwater vehicles. Body and/or Caudal Fin movements (BCF) and Median and/or Paired Fin (MPF) are the main fish swimming modes (Lighthill, 1969; Videler, 1993; Webb, 1994; Sfakiotakis et al., 1999). BCF undulations are the primary propulsion mode used by fishes and can achieve greater thrust and accelerations, while MPF mode is often applied to implement higher swimming efficiency and better maneuverability (Arreola and Westneat, 1996; Sfakiotakis et al., 1999; Triantafyllou et al., 2000; Drucker and Lauder, 2002; Bozkurttas et al., 2009; Lauder, 2015). Thunniform swimming mode is the main BCF movement for fast and efficient swimmers, allowing high cruising speed (6–10L/s, L total length of the fish) for long periods (Mather, 1962; Lindsey, 1978; Dewar and Graham, 1994; Zhang et al., 2020). Their high-performance swimming is due to a streamlined body, crescent-moon caudal fin and finlets (Magnuson, 1978; Shadwick, 2005; Borazjani and Sotiropoulos, 2010; Zhang and Huang, 2022). Apart from the morphological features, Dewar and Graham (1994) and Donley and Dickson (2000) investigated swimming kinematics of tuna by measuring a live tuna in a water tunnel to record the kinematics and named it as thunniform mode. The large amplitude of undulations is primarily restricted to one-half or one-third posterior part of the body while the anterior body undulation is small for thunniform swimmers. Such mode is capable of enhancing the swimming performance (Sfakiotakis et al., 1999; Donley et al., 2004; Smits, 2019). The thunniform mode is not exclusive to tunas or other Scombrid fishes, which also occurs in many different kinds of fast-swimming marine animals, such as cetaceans (Fish, 1998) and lamnid sharks (Donley et al., 2004; Shadwick, 2005).

The outstanding ability of thunniform swimming mode and its potential for providing artificial systems with advanced propeller designs draw scientific attention from various fields. Many experiments with particle image velocity (PIV) techniques provide data on swimming kinematics (Donley and Dickson, 2000) and wake structures (Nauen and Lauder, 2002) of a live swimming fish. However, it is difficult

* Corresponding author at: Key Laboratory for Mechanics in Fluid Solid Coupling Systems, Institute of Mechanics, Chinese Academy of Sciences, Beijing, 100190, China.
E-mail address: yinbo@imech.ac.cn (B. Yin).

https://doi.org/10.1016/j.oceaneng.2023.113866
Received 28 August 2022; Received in revised form 30 October 2022; Accepted 2 February 2023
Available online 15 February 2023

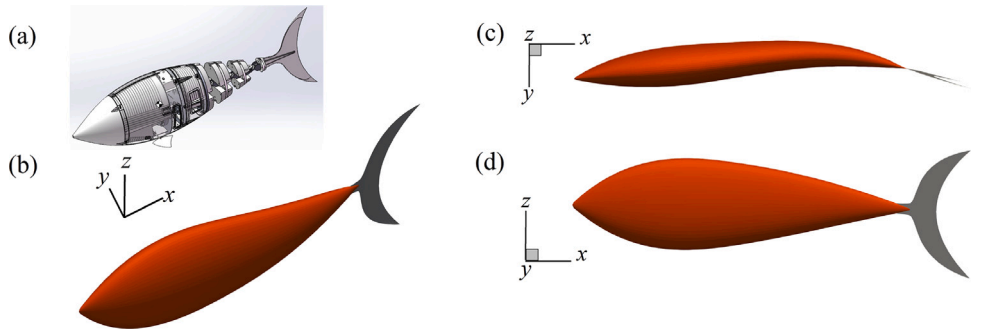

Fig. 1. (a) The CAD model of robotic tuna; (b) Perspective view, (c) $x-y$ plane view, and (d) $x-z$ plane view of the simulation model composed of a streamlined trunk and a high-aspect-ratio crescent caudal fin. The coordinate system is defined as follows: $x-axis$ along the model longitudinal direction to the caudal fin, $y-axis$ along the transverse direction to the right side, $z-axis$ along the spanwise direction, and the $x-axis$, $y-axis$ constitute the right-handed system.

to carry out controlled experiments of various kinematic behaviors for living specimen. Robotic model as an effective tool to study the properties of thunniform swimming is employed to investigate their performance. Triantafyllou and Triantafyllou (1995) built a robotic tuna as an efficient swimming machine and visualized the wake structures to discuss vortex control of tuna swimming. For a robotic tuna, drag reduction and maneuvering performance were also experimentally explored (Barrett et al., 1999; Anderson and Chhabra, 2002). Recently, Zhu et al. (2019) and White et al. (2021) designed a high-frequency robotic tuna based on experimental data from live tunas, which can achieve high undulation frequencies and agree well with tuna kinematics (Shadwick and Syme, 2008). A leading edge vortex (LEV) expected to enhance the thrust was found on the caudal fin of the robotic fish through flow visualization. However, it is difficult to decompose the thrust and drag from the total fluid forces by experiments alone, as well as to estimate the swimming efficiency (Borazjani and Sotiropoulos, 2008, 2009).

To overcome the challenges of experiments, numerical simulations are conducted to investigate the thunniform swimming mechanism. Xia et al. (2015), Li et al. (2017) and Zhang et al. (2020) numerically simulated thunniform swimming mode and performed systematic parametric studies of kinematics. The effect of caudal fin shapes on thunniform swimming has been studied extensively, which came to a consistent conclusion (Chang et al., 2012; Li et al., 2012), i.e., the crescent-shaped fins of tuna exhibit the highest efficiency but generate less thrust. Song et al. (2021) studied the caudal fin transitioning from combined pushing/suction to suction-dominated propulsive mechanism with increasing aspect ratio. Magnuson (1970) proposed that tuna keels act as lift-generating surfaces and enhance longitudinal stability based on their observations of swimming tuna (Euthynnus affinis). Zhang et al. (2020) numerically studied the function of caudal keels on the whole tuna model. Enhancement of thrust and efficiency of the caudal fin was detected with the presence of caudal keels. Using direct numerical simulations(DNS), Zhang and Huang (2022) demonstrated the underlying hydrodynamic mechanism of finlets. They found complex vortices are shedding from the finlets and interacting with each other. In addition, the first two finlets significantly reduce the LEV of the finlets and thus decrease the drag, while the last two finlets reduce the drag of by suppressing the TEV. Moreover, Van Rees et al. (2013, 2015) investigated the morphologies of trunk for fast and efficient undulatory swimmers. The optimal shapes share several features with naturally occurring morphologies, but their overall appearances differ. They identified that the width thickness of the anterior body and the height of the posterior body are critical factors for both speed and efficiency. However, it is still unknown to what extent morphological traits of natural thunniform swimmers are optimized for hydrodynamic performance. Especially, the posterior body shapes make a great difference for the specializations of thunniform kinematics (Sfakiotakis et al., 1999; Smits, 2019).

The objective of current study is to numerically investigate the hydrodynamics of the posterior body morphological traits in thunniform swimming with a yellowfin tuna model (Collette and Nauen, 1983; Xia et al., 2015), whose kinematics is fitted to previous observations (Dewar and Graham, 1994; Zhang et al., 2020). The effects of posterior body shapes on the thrust produced by the caudal fin (CF) and the trunk (TK) drag are elucidated. For comparison, the hydrodynamics of varying height or width of posterior body cross section is discussed. Furthermore, the study examines the effects of the Reynolds number (Re) and the Strouhal number (St) on the hydrodynamic performance. The change scopes of height and width are not so large that they can easily be adopted on robotic tunas, which not only makes the swimming performance differ but also diminishes the design and production costs.

2. Numerical methods

2.1. Reconstruction of tuna model and kinematics

In the present paper, we employ a fish-like autonomous underwater vehicle (AUV) designed in a laboratory presented in Fig. 1(a) as the virtual swimmer, which is made up of a trunk with streamlined profile and a high aspect-ratio crescent caudal fin. Noting that the robotic tuna model is constructed by digitizing the profile of yellowfin tuna (Thunnus albacares) along with the cross-sectional shape, named as CASE(0). All minor fins of the virtual swimmer, such as pelvic, dorsal, anal fins, are neglected. The trunk length is set to 80% of the model total length (L) as shown in Fig. 1, which matches the yellowfin tuna reported in Collette and Nauen (1983), Dewar and Graham (1994) and Xia et al. (2015).

Three-dimensional trunk geometry of the tuna model is reconstructed by orthogonal planar curves for the height and width profiles. Both curves are bijective, continuous and smooth function of the axial coordinates as shown in Fig. 2. For each $x \in [0, 0.8L]$, an elliptical cross-section is defined by half-axes of the width and height curves $y(x)$ and $z(x)$, respectively. The union of cross-sections employs doubly symmetric three-dimensional geometry. The height and width profiles are represented by cubic B-splines with 8 control points. The first and last control points of each curve are fixed at $(x_0^y, y_0) = (x_0^z, z_0) = (0, 0)$ and $(x_5^y, y_0) = (x_5^z, z_0) = (0.8, 0)$, respectively. Only the fourth point $(x/L = 0.6)$ is adjusted, which serves to maintain C^1 continuity at the position linking to the caudal fin and ensure that shape of the anterior body remains unchanged. The caudal fin is treated as two-dimensional deformable membrane structure. The length L_{CF} of CF, measured from fin root to tip along $x-axis$, equals to $0.20L$ and the equivalent surface area S_{CF} is $0.0273L^2$.

The proportion of height variations at this position (the controlled point) is 40% and the proportion of width variations is 40%, as well. We name these cases of varying height with CASE-H(−2), CASE-H(−1), CASE-H(1) and CASE-H(2). The positive value in the bracket means the

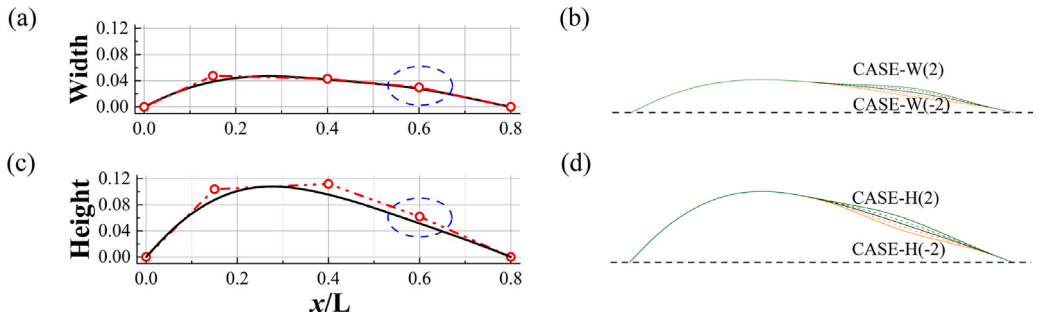

Fig. 2. (a) The width and (c) height profiles (solid black curves) are cubic B-splines defined by the red points for CASE(0); (b) The width and (d) height profiles are width and height variations for posterior body shape, respectively.

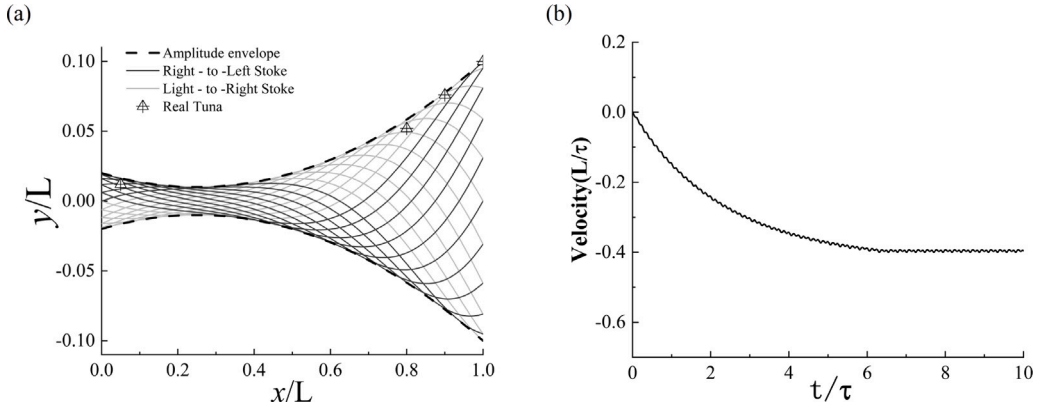

Fig. 3. (a) Midlines of the thunniform swimming mode during undulatory motion; (b) The velocity of the center of mass of the free-swimming model as a function of time, τ is one complete undulation cycle.

height is larger than the CASE(0) while the negative means lower. The cases of width variations is named similarly, e.g., CASE-W(−2), CASE-W(−1), CASE-W(1) and CASE-W(2). Furthermore, we disregard cases in which one or both profile curves cross the trunk midline.

The present study performs high-fidelity simulations for the model with prescribed kinematics. The model is a three-dimensional (3D) yellow fin tuna-like flexible body undulating with prescribed experimental kinematics of thunniform type. The prescribed kinematics for the body/caudal fin is in the form of a backward traveling wave (Dewar and Graham, 1994; Zhang et al., 2020), with the wave amplitude varying from the head to the tail. We describe the lateral undulation motion by the following expression, which has been adopted in previous numerical studies (Borazjani and Sotiropoulos, 2008; Zhang et al., 2020):

$$y(x,t) = A(x)\sin(kx - \omega t), \tag{1}$$

where $y(x,t)$ is the lateral excursion of the midline at time t, x is the axial direction measured from the head to the tail tip, the amplitude envelope of lateral motion is $A(x) = a_0 + a_1 x + a_2 x^2$, with the coefficients $a_0 = 0.016$, $a_1 = -0.066$ and $a_2 = 0.15$, which are carefully determined according to the experimental data of thunniform swimming mode to achieve the specified values of the wave amplitude. $k = 2\pi/\lambda$ is the wave number of the body undulations, λ is the wavelength and selected as $1.25L$ (L is the total body length), in the range of $1.23L$–$1.29L$ suggested by previous observations of tuna (Xia et al., 2015; Khalid et al., 2021), and $\omega = 2\pi f$ is the angular frequency, where f is the caudal fin beat frequency. For the undulation frequency, our simulations are carried out for $f = 4$ Hz in the range of 1.4–5.2 Hz for the 53 cm yellow fin tuna group and 50 cm Pacific mackerel reported by the experimental results (Dewar and Graham, 1994). A sequence of midlines for the current tuna model during one undulation cycle are plotted in Fig. 3(a).

2.2. Simulation approach

In the natural environment, the propulsion performance is principally governed by two key dimensionless parameters, the Strouhal number (St) and the Reynolds number (Re). The Strouhal number is defined as:

$$St = \frac{f A_m}{U_\infty}, \tag{2}$$

where A_m is the maximum undulatory amplitude of caudal fin and U_∞ is the velocity of incoming flow. St represents the ratio of the transverse undulatory velocity to the advance velocity. To choose the St for studying the effects of posterior body shapes, a self-propelled tuna model (CASE(0)) is simulated to determine U_∞. The degree of freedom for the tuna swimming is restricted in the streamwise direction only. Fig. 3(b) shows the time history of streamwise velocity of the center of mass. The tuna swimming speed reaches a periodic state and the cycle-averaged speed is $0.4L/\tau$. So the Strouhal number is set as 0.5, falling within the range of experimental for tuna and efficient swimming propulsion in nature. Zhang et al. (2020) studied the hydrodynamic characteristics and vortex wake structures for $St = 0.18 - 0.72$. The Reynolds number represents the ratio of inertial force to the viscous force, defined as follows:

$$Re = \frac{U_\infty L}{\nu}, \tag{3}$$

where ν is the kinematic viscosity. It is difficult to directly simulate the flow at a high Re by current computational method although Re of fish swimming is in the order of 10^4–10^5 (Liu et al., 2017). $Re = 10^3$ is adopted according to the previous works (Borazjani and Sotiropoulos, 2008, 2009, 2010; Liu et al., 2017), which show that, the fish swimming is inertia-dominated and the results do not change significantly. The range of Re can help to understand the predominant vortex dynamics and capture the key features of the wake structures to address the

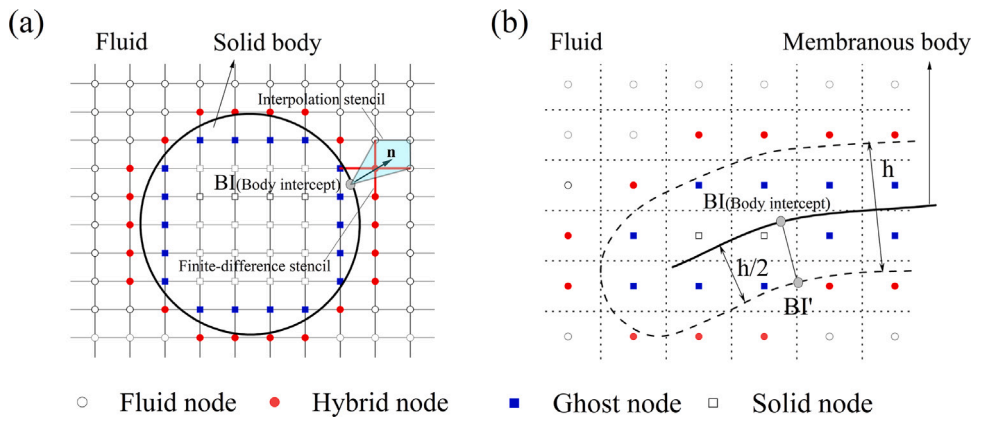

Fig. 4. (a) A schematic illustrating the immersed-boundary method used in the present solver. The mixed interpolation/finite-difference stencil for the hybrid nodes defined inside the fluid region. The cross in (a) represents the second-order central difference stencil. The shaded areas are the support regions for the interpolating polynomials. (b) A schematic showing the artificial thickness of a membranous body.

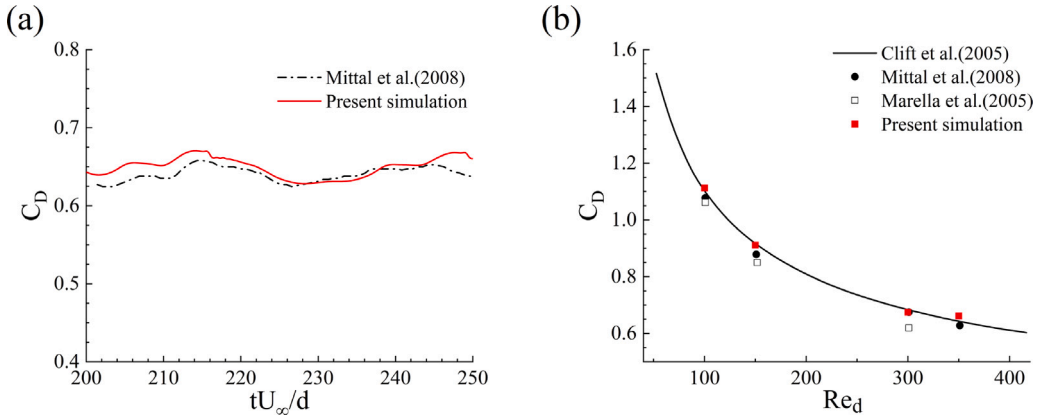

Fig. 5. (a) Temporal variation of drag coefficient on a sphere in a uniform flow for $Re_d = 350$. (b) Comparison of computed mean drag coefficients with experimental and numerical data.

fundamental hydrodynamic mechanisms of tuna swimming. To solve fluid–structure interaction problems with largely displaced/deformed moving boundaries, a finite-difference-based Cartesian grid immersed-boundary method is adopted.

2.2.1. Numerical simulation method

The 3D incompressible viscous Navier–Stokes equations govern the fluid dynamics around the swimmer, written in indicial form as:

$$\frac{\partial u_i}{\partial x_i} = 0 \tag{4}$$

$$\frac{\partial u_i}{\partial t} + u_j \frac{\partial u_i}{\partial x_j} = -\frac{1}{\rho}\frac{\partial p}{\partial x_i} + \frac{1}{Re}\frac{\partial}{\partial x_j}\left(\frac{\partial u_i}{\partial x_j}\right), \tag{5}$$

where $i, j = 1, 2, 3$, u represents the Cartesian components of the fluid velocity, x donates a Cartesian direction, ρ the fluid density and p the pressure. The incompressible Navier–Stokes equations are discretized adopting a cell centered collocated arrangement of primitive variables and solved using a finite-difference-based Cartesian grid immersed-boundary method. It is a method for addressing fluid–structure interaction problems with largely displaced/deformed moving boundaries. The spatial terms are discretized using a second-order central difference scheme. The equations are marched integrated in time using a variation of Chorin's projection–correction approach, and the Crank–Nicolson scheme is used to discretize all the terms of the momentum equation in the conservative form. The method adopts a multi-dimensional ghost-cell methodology to satisfy the boundary conditions on the immersed solid boundaries. The fluid–solid interface is represented by a set of Lagrangian marker points and three-node triangular elements. To implement the boundary conditions at the interface, 'ghost nodes' outside the fluid region are defined at each time step, at which the flow variables are extrapolated (Mittal et al., 2008). To suppress the numerical oscillations that may happen when solving a moving boundary problem, hybrid nodes shown in Fig. 4(a) are defined inside the fluid region, at which the flow variables are weighted averages between the interpolated solution and the solution to the Navier–Stokes equations.

In biological locomotion problems of fish swimming, one often has to deal with thin bodies, e.g., fins, whose thickness is much smaller compared to the characteristic length of the body. Such membranous bodies are often modeled as zero-thickness structures. The vanishing thickness in this case will cause the present method to fail, since a ghost node is also a fluid node at the same time. The problem is circumvented by introducing a uniform artificial thickness, h, along the membranous body. Nodal points whose distance to the membrane is less than $h/2$ are defined as solid nodes, and the rest nodal points are fluid nodes. Once the 'interior' and 'exterior' regions are determined, the ghost and hybrid nodes can be easily identified in the same way as a regular body. To construct the interpolation and extrapolation stencils for the hybrid and ghost nodes, the body intercepts of the nodes with inflated surface are needed. Without a mesh representation of the inflated surface, we compute the nearest point on the physical boundary for each hybrid or ghost node, and the point is defined as the true body intercept (BI) of the hybrid or ghost node. Then the pseudo BI point (BI′) for a hybrid node is found by truncating $h/2$ off the line connecting the BI and the hybrid node, and for a ghost node, BI′ is found by extending the line from the BI to the ghost node to $h/2$ (Fig. 4(b)). Since h is small, we

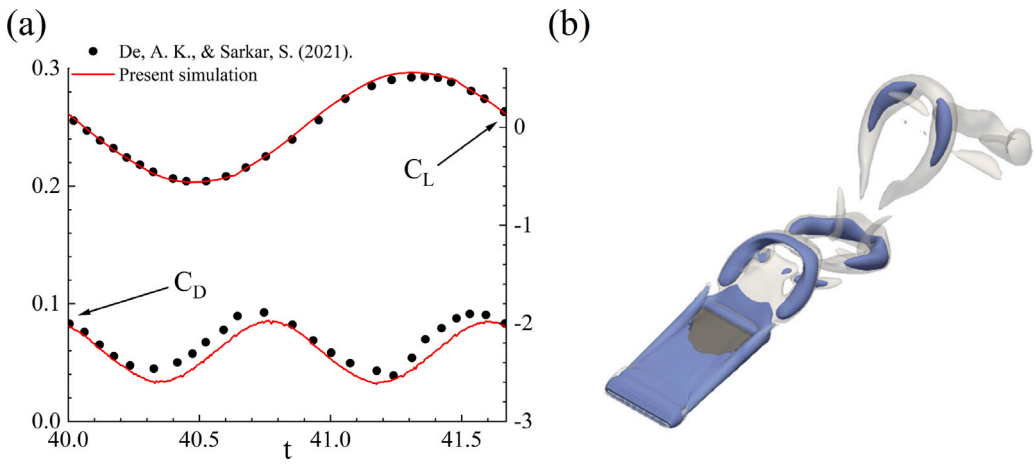

Fig. 6. (a) Temporal variation of drag coefficient (C_D) and lift coefficient (C_L). (b) Perspective view of the 3D instantaneous vortical structures visualized by the Q-criterion ($Q = 1$).

assume that the boundary conditions at the BI are the same as those at the corresponding BI′. After extending the thickness, the membranous body can be treated in the same manner as a regular 3D body. In the present solver, h is typically chosen to be around three cells wide. Thus, the artificial thickness is automatically decreased as the grid is refined.

More detailed descriptions about the solvers can be found in Luo et al. (2010, 2012) and Yin et al. (2019). Such method has been successfully applied to simulate the fluid dynamics of low to intermediate Reynolds number flow (Liu et al., 2017; Han et al., 2020; Khalid et al., 2021).

2.2.2. Validation of numerical simulation method

In addition to the validation tests described in previous publications for the current numerical method, two other tests are performed here. The first test concerns a uniform flow over a rigid sphere with stationary immersed boundary. We have performed simulations with Reynolds numbers ranging from 100 to 350 and made qualitative as well as quantitative comparisons with established data. The Reynolds number defined as: $Re_d = (U_\infty D)/\nu$, where D represents the sphere diameter. These simulations run for long enough time period so as to reach a well established stationary state. Fig. 5(a) shows the temporal variation of the drag coefficient for case $Re_d = 350$ and the flow quantity clearly show that the flow has reached a stationary state. The drag coefficient curve of present simulation is found to be nearly consistent with the result in Mittal et al. (2008). Furthermore, we compare the computed mean drag coefficient with a number of previous experimental and numerical studies in Fig. 5(b) and find that the values match quite well with these past studies (Clift et al., 2005; Marella et al., 2005; Mittal et al., 2008).

The second validation test is a moving-boundary problem. The physical problem involves the pitching of a thin rectangular rigid panel about its leading edge, placed in a uniform flow. The pitching motion is described by the angular displacement $\theta(t) = \theta_{max}\sin(2\pi f t)$, where f is the pitching frequency and the maximum angular displacement is given by $\theta_{max} = \arctan(A/2C)$, where A and C are the double pitching amplitude of the panel trailing edge and chord length of the panel, respectively. The control parameters for the problem are the aspect ratio given by the span (S)-to-chord (C) ratio $AR = S/C$, the Reynolds number and Strouhal number based on chord $Re = (U_\infty C)/\nu, St = (fC)/U_\infty$. We limit $\theta_{max} = 5°$, $AR = 0.54$, $Re = 1000$ and $St = 0.6$. The 3D simulation is conducted in a $10C \times 8C \times 8C$ (in the streamwise, transverse, and spanwise directions) domain and on a $451 \times 301 \times 201$ non-uniform grid with grid clustering provided around the pitching plate and in the near wake, which is similar to De and Sarkar (2021). Fig. 6(a) shows temporal evolution of the coefficients of lift C_L and drag C_D, which defined as $C_{L,D} = F_{L,D}/(1/2\rho U_\infty^2 SC)$, where F_L, F_D are the lift and drag components acting on the panel, respectively. The curves match well with the numerical results of reference. Moreover, perspective view of the three dimensional instantaneous vortical structures visualized by the Q-criterion shows a very good agreement between present simulation in Fig. 6(b) and De and Sarkar (2021). Given the complexity and difference in the solution technique of the references, results obtained by our numerical simulation method are found to be in the range of excellent to reasonable.

2.2.3. Grid convergence verification

As shown in Fig. 7(a), the entire domain size is $8L \times 5L \times 5L$, which is large enough to obtain accurate and converged results. The complex immersed body surfaces are represented by grids consisting of unstructured triangular elements. The trunk surface is made up of triangular unstructured meshes, with 4802 node points and 9600 elements for the trunk and 775 node points and 1440 elements for the caudal fin in Fig. 7(b). The model surface is set as the no-slip and no-penetration boundary condition. The flow is simulated with the non-uniform Cartesian grids. The grid is refined around the tuna model, and this cuboidal region size is $2L \times 0.5L \times 0.5L$ with high-resolution $\Delta = 1/200$ in each dimension to confirm that the simulation results are grid independent. The total number of grids in the computational domain is $411 \times 181 \times 181$(approximately $13.5million$) grid points in total. The inlet on the left(upstream boundary) is set as the constant velocity boundary condition and a homogeneous Neumann boundary condition is used for the pressure; the outlet on the right(downstream boundary) is set as the zero gradient boundary condition for both the velocity and pressure; and other boundaries are set as zero-stress boundary conditions. Fig. 7(c) shows the comparison of the thrust coefficients of caudal fin at $Re = 6400$ and $St = 0.5$ for three meshes: (1) a coarse mesh $\Delta = 1/150$; (2) a medium mesh $\Delta = 1/200$; (3) a fine mesh $\Delta = 1/250$. These cases of tuna swimming are simulated using a time step of $\Delta t = 1 \times 10^{-3}$, resulting in $CFL \leq 0.5$. It is observed that the difference of either the mean value or the peak value of the thrust coefficient between the medium and the fine grid cases is less than 1.8% in Fig. 7(c). So the medium grid is chosen in the simulations to achieve computing accuracy and economy.

Once the flow field is solved, the surface pressure and shear force on the model trunk and caudal fin are projected from the flow variables around the tuna and integrated to compute the forces, i.e., $\oiint(\sigma \cdot \mathbf{n})ds$. The power consumption P is calculated from the integration along the model surface, defined as:

$$P = -\oiint(\sigma \cdot \mathbf{n}) \cdot \mathbf{V} ds, \tag{6}$$

where σ is the stress tensors, $\mathbf{n}$ represents the normal vector of each point on the model surface and $\mathbf{V}$ donates the velocity vector of the

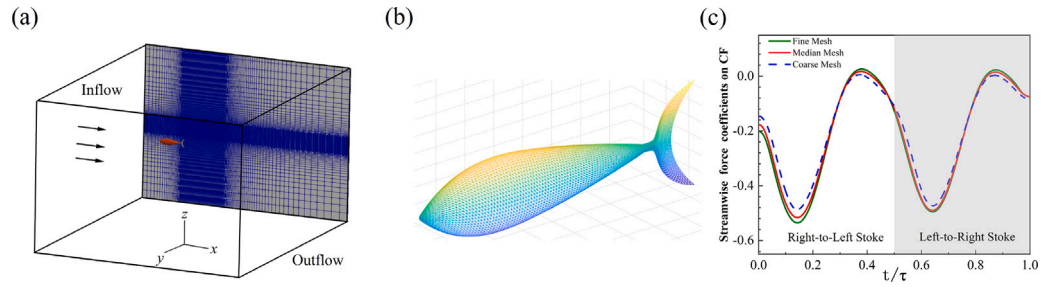

Fig. 7. (a) Schematic of the computational mesh and boundary conditions; (b) The perspective view of unstructured surface mesh for the tuna model; (c) Comparison of the streamwise force coefficients on caudal fin for demonstration of the grid independence.

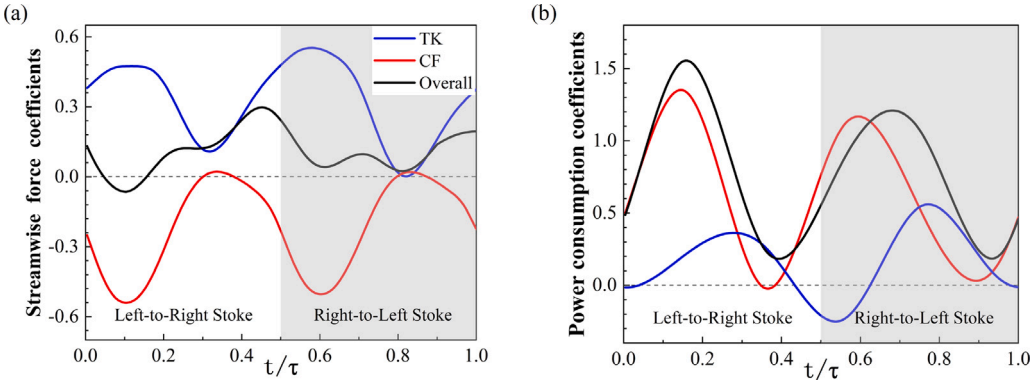

Fig. 8. Time history of (a) streamwise force coefficients and (b) power consumption coefficients of the CASE(0) model during one representative undulatory cycle. The blue, red and black solid lines in (a) and (b) are streamwise force and power generated by trunk(TK), caudal fin(CF) and the total, respectively.

fluid. We adopt two nondimensionalized coefficients(C_F and C_P) to represent the streamwise force and the power consumption denoted as follows:

$$C_F = \frac{F}{1/2\rho U_\infty^2 S_{CF}}, C_P = \frac{P}{1/2\rho U_\infty^3 S_{CF}}, \tag{7}$$

where ρ represents the fluid density. Furthermore, the positive direction of the streamwise force is defined to be same as that of the incoming flow, i.e., the positive x-direction. So for the fixed model confronting an incoming flow, positive and negative streamwise forces are drag and thrust, respectively. The coefficients are denoted as C_D(drag of trunk) $= C_F$ and C_T (thrust of caudal fin) $= -C_F$. In addition, the swimming efficiency(Froude efficiency) is defined as:

$$\eta = \frac{\bar{C}_T \tilde{U}}{\bar{C}_P}. \tag{8}$$

where $\bar{C}_T$ and $\bar{C}_P$ represent the cycle-averaged thrust coefficient and power coefficient, respectively. $\tilde{U}$ is the scaled average velocity as $\tilde{U} = U/U_\infty$. Three dimensional wake structures are then visualized by the iso-surface of the $Q-criterion$ (Hunt et al., 1988) which identifies flow regions where rotation dominates over strain. The quantity Q is defined as:

$$Q = \frac{1}{2}(\left\|\Omega^2 - S^2\right\|). \tag{9}$$

where Ω and S are the symmetric and antisymmetric parts of the velocity gradient, respectively. $\|\cdot\|$ is the Euclidean matrix norm. The rotation rate dominates the strain rate, and are occupied by vortical structures where $Q > 0$.

This method works well to solve bio-inspired fluid–structure problems for both rigid and membranous structures. The advantage of this computational solver is the ability to settle large-amplitude oscillations of complex-shaped bodies and membranous structures, and their interaction with surrounding fluid. Because numerous parameters cannot be controlled with live tuna in laboratory conditions, our numerical simulations allow the researchers to have more freedom to prescribe different kinematic profiles over tuna-like anatomical models and examine their hydrodynamic performance.

3. Results and discussion

In this section, we first present the simulations of the tuna model with different posterior body shapes at $Re = 6400$ and $St = 0.5$, and then the effects of Re and St numbers are analyzed.

3.1. Hydrodynamic forces and wake topology of the original case

In this part, the simulation results, including the hydrodynamic performance and vortex structures of the computational model are presented. In all numerical simulations, the results are taken from the 6th cycle when the flow field reaches a steadily periodic state. Fig. 8(a) shows the time series of streamwise force coefficients produced by the trunk(TK) and the caudal fin(CF). It indicates that CF generates thrust, while TK mainly produces drag during the whole undulatory stroke. Two peaks appear in the caudal fin thrust curve, and similar situation happens to the drag curve. An interesting observation in Fig. 8(b) is that for tuna model the power consumed by trunk becomes negative at some intervals during the undulatory cycle, consistent with the previous studies (Borazjani and Sotiropoulos, 2010; Wang et al., 2019). Fig. 8(b) also shows that two peaks arise in the power consumption by the CF, which lag slightly behind the corresponding peaks in the thrust depicted in Fig. 8(a). The cycle-averaged streamwise force $\overline{C}_{F,0}$ and power consumption $\overline{C}_{P,0}$ are tabulated in Table 1. The subscript '0' in $\overline{C}_{F,0}$ and $\overline{C}_{P,0}$ represents the original CASE(0). It is found that CF consumes the majority 77% of the total hydrodynamic power output.

Fig. 9(a)(b) show the 3D instantaneous wake topology of CASE(0) when the caudal fin reaches the leftmost position and starts to move back to the opposite side. We find two sets of interconnected vortex rings are produced in the downstream region and convect to the downstream. This coincides with the double row wake structures described

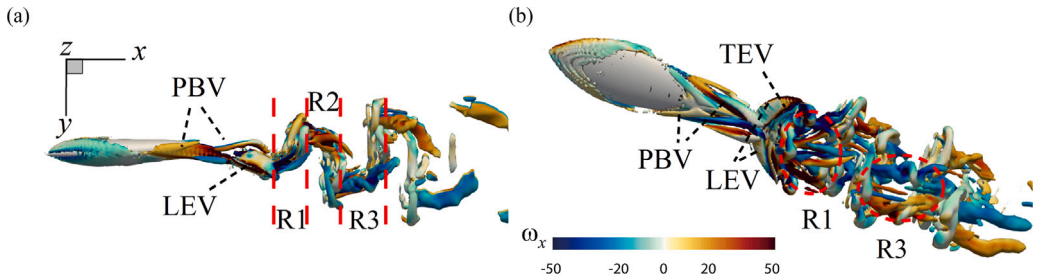

Fig. 9. Three-dimensional instantaneous wake structures in CASE(0) from (a) top view and (b) perspective view. The coherent structures are colored by the isosurface $Q = 50$ of the Q-criterion. The isosurface is colored by the x-component of vorticity ω_x.

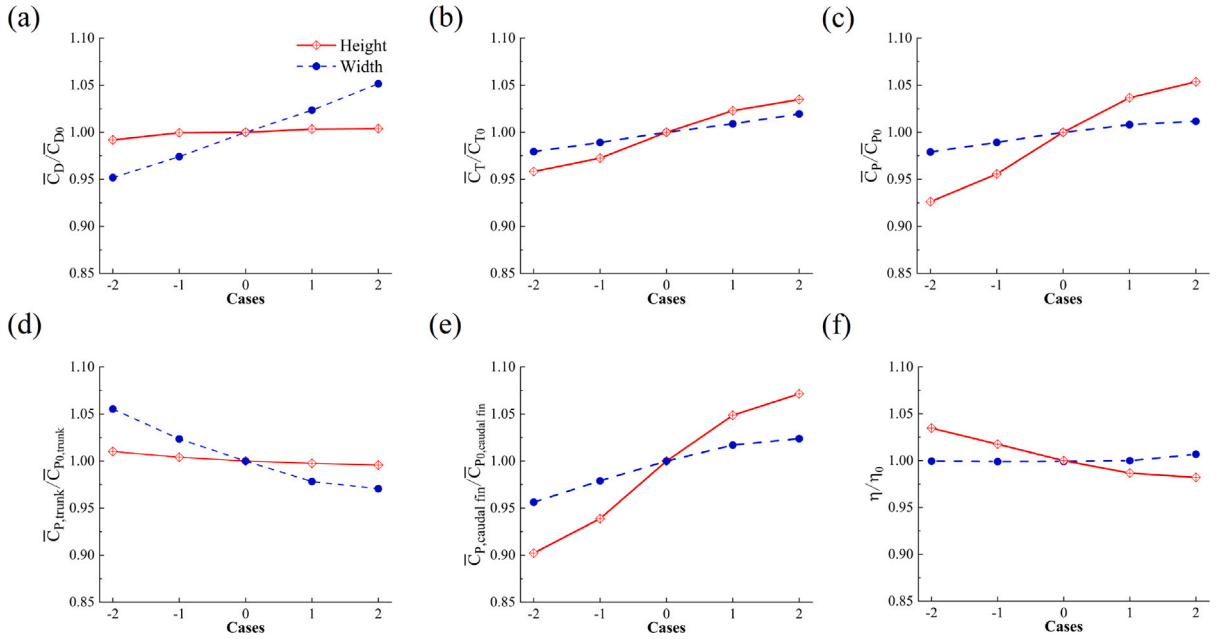

Fig. 10. (a) Drag coefficients of TK, (b) thrust coefficients of CF, power consumption coefficients of (c) the whole model, (d) TK and (e) CF, and (f) the efficiency, where each cycle-averaged coefficient is normalized by its respective value of CASE(0). The blue dashed lines and red solid lines are the trends of varying width and height. The subscript 'trunk' and 'caudal fin' represent hydrodynamic properties generated by the trunk and caudal fin.

Table 1
Cycle-averaged streamwise force $\overline{C}_F$ and power consumption $\overline{C}_P$ produced by TK and CF of CASE(0).

	$\overline{C}_{F,0}$	$\overline{C}_{P,0}$	η
TK	0.323	0.1844	–
CF	−0.2125	0.618	–
Total	0.1105	0.8024	43.05%

in previous papers (Saadat et al., 2017) at $St > 0.3$. Furthermore, many small-scale vortices produced from the posterior body emerge with the vortex rings. As observed in Fig. 9, vortices are generated in the posterior region of the tuna model body. These vortices are termed as PBV_s. In addition, vortices generated by the leading edge and trailing edge of the caudal fin are termed as LEV_s and TEV_s, respectively. Moreover, interconnected vortex rings ($R1$ to $R3$) merged by these vortices are shed from the caudal fin during the undulatory motions. The vortex rings are labeled in chronological order with a smaller index number for more newly generated vortex rings. The PBV_s move towards the peduncle region, and then interact with LEV_s formed around the caudal fin, which further affects the strength of the LEV_s. It is important to notify that PBV_s change with varying posterior body shapes, whose effects on swimming performance will be discussed later.

3.2. Comparison of varying posterior body shapes

Following the same motion mode and simulation set-up as in the previous section, the effects of posterior body shapes have been investigated. Red solid lines in Fig. 10(a)(d) show that the trunk drag and power consumption curves remain almost flat with the height change, although the model volume has been altered. The caudal fin thrust improves from 95.8% to 103.5% compared with CASE(0) and the power consumption of the caudal fin changes from 90.2% to 107.1% as the height increases in Fig. 10(b)(e). It is found in Fig. 10(c)(f) that the total power consumption increases, while the efficiency shows 5% reduction from CASE-H(−2) to CASE-H(2). On the other hand, as the width increases(blue dashed lines in Fig. 10), the caudal fin thrust and power consumption change less compared with height effect. However, the trunk drag increases with the trunk power consumption reduced by 8.2%. From CASE-W(−2) to CASE-W(2), the efficiency of tuna swimming experiences slight increase. In general, thrust is more sensitive to posterior body height change, while drag more sensitive to width modification. Height increase could enhance thrust and reduce efficiency, while width enlargement improves the drag and efficiency.

3.2.1. Posterior body height

To provide comprehensive comparison of the hydrodynamic performance, the time history of C_D, C_T and C_P are shown in Fig. 11 (regarding height variation) and Fig. 15 (regarding width variation).

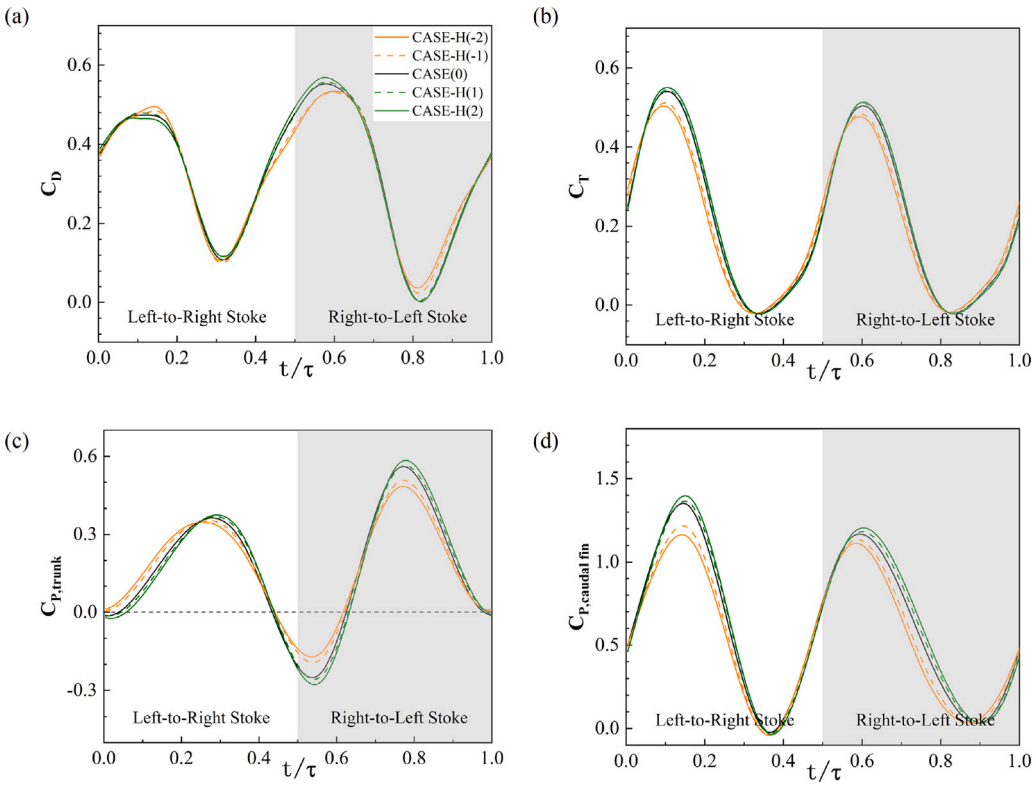

Fig. 11. Time histories of: (a) drag coefficients of TK, (b) thrust coefficients of CF, power consumption coefficients of (c) TK and (d) CF of varying height during one whole undulatory cycle.

In Fig. 11(a), as height increases, the peak-to-valley amplitude of C_D enlarges during right-to-left stroke and changes little in reversal stroke. So the difference of cycle-averaged drag for these models is not evident. In addition, the trunk consumes more energy and harness more hydrodynamic power from flow in the whole undulatory cycle as height increases in Fig. 11(c). Caudal fin undulates to its leftmost and rightmost position at $t/\tau = 0$ and 0.5. The thrust reaches maximum at $t/\tau = 0.12$ and 0.6 for CASE(0), which is similar for other cases in Fig. 11(b). From CASE-H(−2) to CASE-H(2), the two peaks of thrust and power coefficients generated by CF have been enhanced while the valleys keep almost unchanged around zero as shown in Fig. 11(b) and (d). It conforms to Fig. 10(b) and (e) that increase of posterior body height produces more thrust and power consumption.

Fig. 12 presents instantaneous 3D wake structures of CASE-H(−2), CASE(0) and CASE-H(2). In all cases, PBV_s and LEV_s are generated periodically by the upper and lower edges of the posterior body. Some smaller-scale vortex is separated from the PBV as caudal fin undulates, denoted as PBV_B which was formed in last stroke. At the beginning of this undulatory stroke, PBV_L is attached to the posterior body. Then as CF moves rightward, PBV_L moves down to the peduncle region and a new vortex tube PBV_R is formed. And the new tube PBV_R has the opposite direction to PBV_L. The subscripts 'R' and 'L' mean the vortices generated in the left-to-right and right-to-left stroke, respectively. In addition, PBV_L gradually forms LEV_R and LEV mainly attaches to the CF right side surface. Part of the previous PBV_R and the vortex shed from the posterior body merge to a new vortex tube, which is named as PBV_{BR} and directly merges with the vortices generated by the trailing edge (TEV) in Fig. 12. Later on, LEV_R covers the whole CF left side surface in Fig. 12(a), (d) and (g). Then PBV_R reaches the root region of CF, and LEV is generated on the CF right side surface in Fig. 12(b), (e) and (h). Similar vortex compression of the PBV_s can be found in Zhu et al. (2002) and Liu et al. (2017). Meanwhile, LEV_R covering the CF left side surface moves down along the CF surface and finally merges with the vortices generated by the trailing edge. Such vortex merging forms a large TEV shedding from the trailing edge of CF. This TEV, together with the previous shed TEV, forms a vortex ring and then convects downstream. When CF reaches the rightmost, PBV_R is fully developed and attached to the posterior body. The rest PBV_L merges with the previous vortex separated from the posterior body to form a new PBV_{BL}. It can also be seen that the strength of PBV_B for CASE-H(2) in Fig. 12(i) is much stronger than that formed in CASE(0) and CASE-H(−2) at $t/\tau = 0.6$. We also observe that PBV_{Bs} become stronger as height increases, indicating stronger vortices separated from the trunk and are not applied to generate LEV, which reduces the efficiency. The 3D wake structures show that the swimming performance of the caudal fin may be enhanced due to the stronger PBV_s generation and interaction of PBV_s and LEV_s, which strengthens LEV_s.

In order to better illustrate the vortex strength and vortex–vortex interaction near the root region of the caudal fin, vertical and horizontal slices cutting through the flow field in Fig. 12 near CF root region are displayed in Figs. 13 and 14. In Fig. 13(a)(b)(c), it can be seen that PBV_L and PBV_{BR} both become stronger as height increases during the left-to-right stroke. PBV_{BL} partly merge with PBV_L and this interaction is constructive to enhance PBV_L at the CF root region, which can be strengthened by height increase. During the reversal stroke, the constructive interaction between PBV_{BR} and PBV_R also arises and occurs more evidently for CASE-H(2), compared to CASE(0) and CASE-H(−2) in Fig. 13(f). It is observed that the strength of PBV_L and PBV_R are stronger as height increases in Fig. 13 showing the contour of ω_x in CF root region. In addition, PBV_{BL} has been generated in Fig. 13(f), which is not weak and unnoticeable at the same time in Fig. 13(d) and (e). Result suggests that the strength of PBV_{Bs} grows as height increases, which may consume more power.

Fig. 14(a)(b)(c) show the horizontal slice of the ω_z contour. LEV_s for both sides of the caudal fin grows with larger height, meaning that stronger PBV_s can strengthen the trunk-fin interaction. Circulation of vorticity ω_x from LEV attached to the CF left side during half stroke

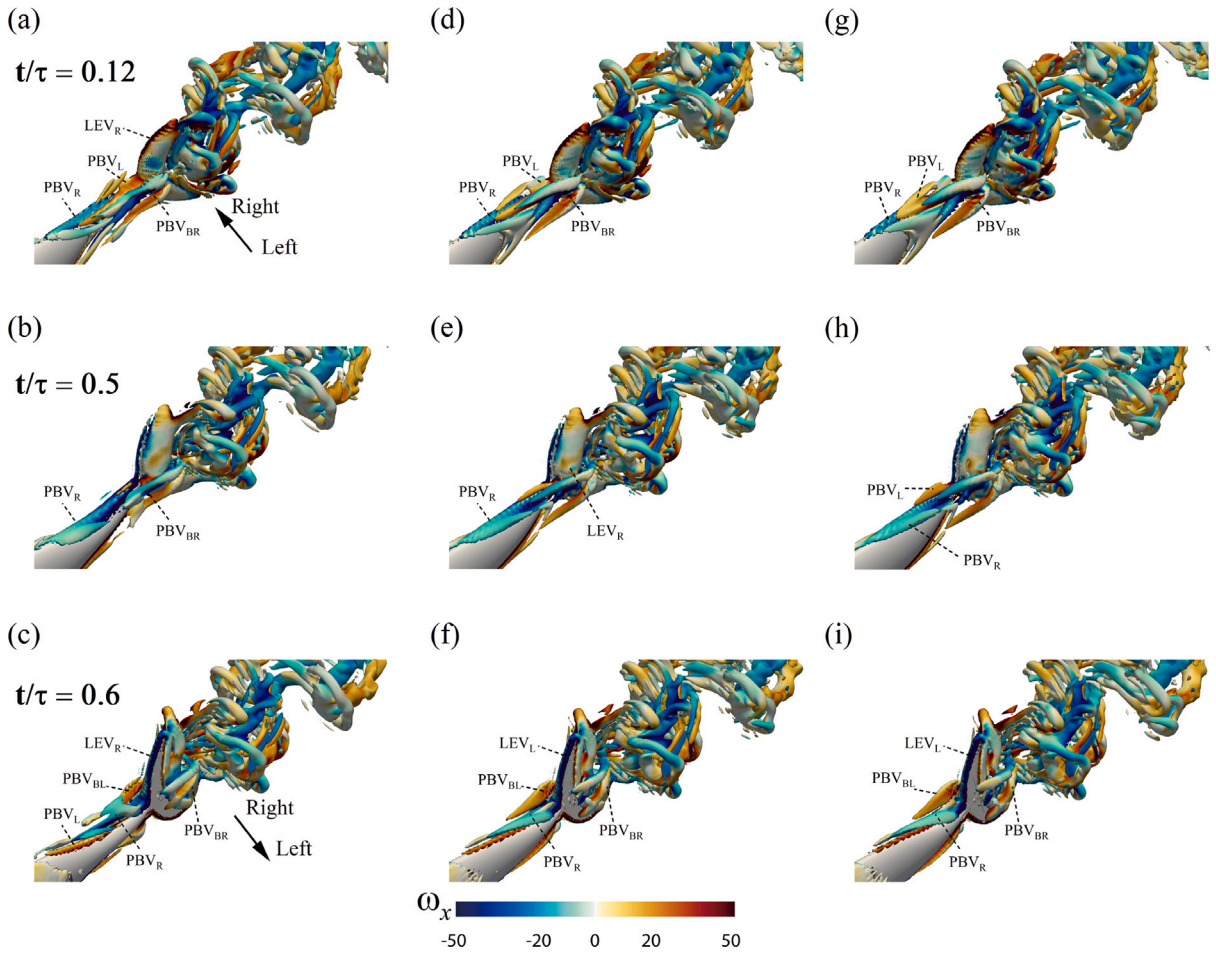

Fig. 12. Instantaneous three-dimensional wake structures of tuna models with different posterior body height: (a)(b)(c) CASE-H(−2), (d)(e)(f) CASE(0) and (g)(h)(i) CASE-H(2) at (a)(d)(g) $t/\tau = 0.12$, (b)(e)(h) $t/\tau = 0.50$, (c)(f)(i) $t/\tau = 0.6$. The coherent structures are visualized by the iso-surface $Q = 50$ of the Q-criterion and colored by x−component of vorticity ω_x.

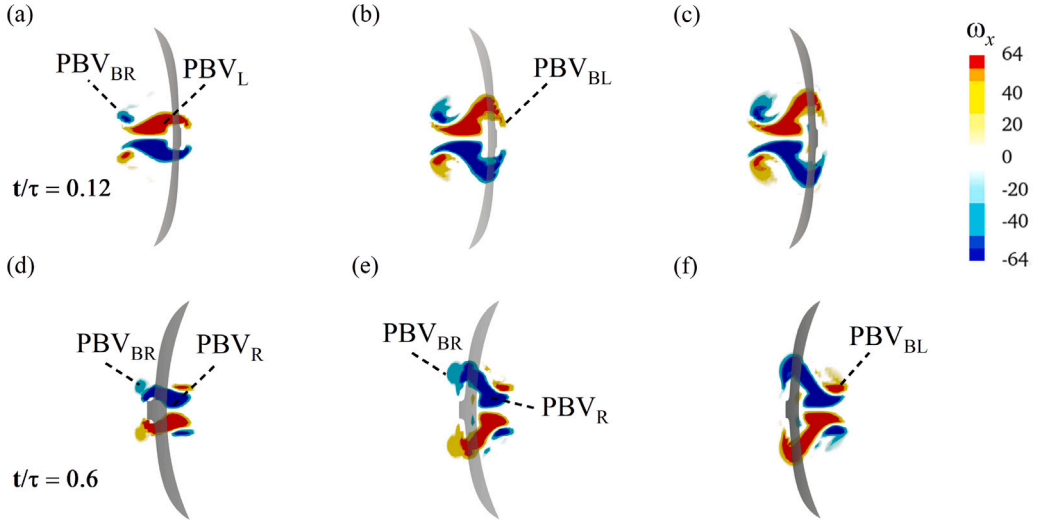

Fig. 13. Contour of normalized ω_x on a vertical plane located at $0.80L$ on the caudal fin root region cutting through the flow field of (a)(d) CASE-H(−2), (b)(e) CASE(0) and (c)(f) CASE-H(2).

is quantified to compare the LEV strength among different cases in Fig. 14(d). Circulation (Γ) of vorticity is defined as:

$$\Gamma = \oint \mathbf{V} \cdot dl \tag{10}$$

Once the vorticity field is visualized and each vortex is identified, a closed contour line with 40% of the maximum vorticity value is set around the LEV (Liu et al., 2017; Han et al., 2020). The circulation is computed along this contour line. Fig. 14(d) displays the temporal

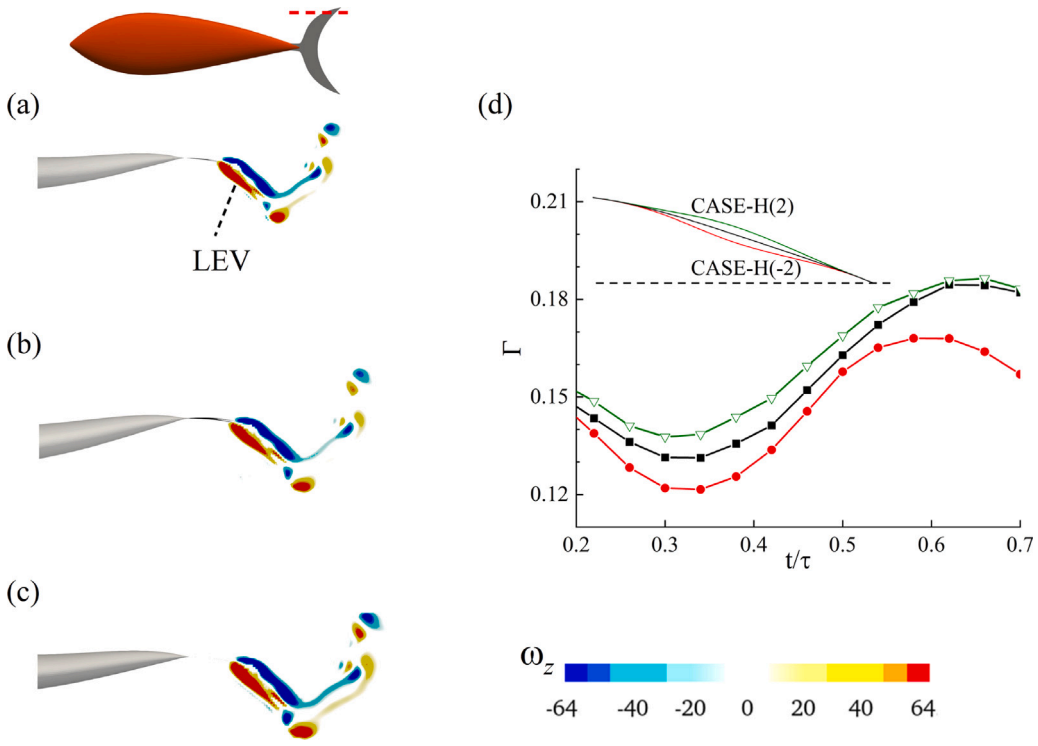

Fig. 14. Contour of normalized ω_z on a horizontal slice of the top CF leading edge at $t/\tau = 0.12$ cutting through the flow field of (a) CASE-H(−2), (b) CASE(0), and (c) CASE-H(2). (d) Circulation (Γ) of vorticity ω_z from the LEV attached to the leftside of CF surface on the slice, whose position is through the top CF leading edge.

comparison of the LEV circulation value on the horizontal slice cutting through the top of caudal fin. The results show that these cases share the same trend and LEV circulations are enhanced during the whole undulation stroke with increased height, which agrees with the instantaneous force change in Fig. 11 and explains why larger caudal fin thrust occurs in CASE-H(2).

3.2.2. Posterior body width

It is noticeable that increased width mainly generates more trunk drag. Fig. 15(a) presents that the peak of trunk drag enhances as width expands, while the valley value remains unchanged. Although the curves of trunk power consumption in Fig. 15(c) are close to each other, the trunk consumes less power and harnesses more from the flow with larger width. From CASE-W(−2) to CASE-W(2), it is indicated that two peaks of thrust and caudal fin power coefficients increase while the valleys remain the same in Fig. 15(b)(d). Moreover, peaks or valleys of these coefficients all rise at the same moment.

It is observed that major part of PBV_L is attached to the left side of trunk for CASE-W(−2) in Fig. 16(a) while weaker PBV_L for CASE-W(2) in Fig. 16(b), which is attribute to the weakened interaction between PBV_R and PBV_L. Difference of PBV_s is also more evident for CASE-W(−2) at $t/\tau = 0.6$. PBV_s attached to the left and right side of trunk lead to low and high pressures acting on the trunk surface, resulting in suction and pushing forces, respectively, and a forward force component is generated to overcome the drag. Therefore, the pressure difference between the two sides of posterior body resulting from PBV_s helps diminish the trunk drag. In addition, PBV_{BL} and PBV_{BR} are weaker as width increases in Fig. 16, slightly improving efficiency.

Fig. 17(c) shows that stronger PBV_L related to the contours of ω_x arises for CASE-W(2) in the CF root region than CASE-W(−2) at the early stage, which suggests increased width can also enhance thrust. Besides the PBV_L, it is also observed that PBV_{BR} on the CF left side in Fig. 17(a)(c) and PBV_{BR} weakens as width increases. In Fig. 17(b)(d), PBV_{BR} merges more with PBV_R for CASE-W(2) and this interaction strengthens PBV_R at $t/\tau = 0.6$, which boosts the thrust generation. In terms of circulation of vorticity ω_z from LEV shown in Fig. 17(e), the strength in CASE-W(2) is much higher than other cases during a certain interval. Meanwhile LEV does not change obviously for the rest time in half stroke, corresponding to the caudal fin thrust coefficients curve in Fig. 15(b).

Contours of pressure distributions from a horizontal slice through the mid-span of tuna model are plotted in Fig. 18. We further explore the causes of pressure difference due to PBV_s attached to the left and right sides of the trunk. The pressure coefficient is defined as:

$$\tilde{p} = \frac{p - p_\infty}{1/2\rho U_\infty^2}, \tag{11}$$

where p_∞ is the pressure of free stream. As the model undulates, pressure regions with oscillating positive- and negative-pressure gradients alongside the posterior body and caudal fin also appear, resulting from the production and transfer of PBV_s. According to Fig. 18, the anterior bodies in all cases do not exhibit a large pressure difference between the left and right sides. At the instant of the maximum trunk drag peak during each half stroke, the pressure difference between two sides of the posterior body for CASE-W(−2) is higher than CASE-W(2). Meanwhile, at $t/\tau = 0.31$ and $t/\tau = 0.83$, the pressure difference changes little for the two cases in Fig. 18, corresponding to the valley of trunk drag coefficients in Fig. 15(b) during each half stroke.

3.3. Effect of the Reynolds number

The undulatory propulsion performance is principally governed by the Reynolds number and the Strouhal number. We keep $St = 0.5$ and examine the effects of Re from 1600 to 8000, which spans the transitional and inertial regimes. CASE-H(−2), H(2), W(−2) and W(2) are taken into consideration. As plotted in Fig. 19(a)(b), it is observed that when Re grows the cycle-averaged trunk drag distinctly decreases while the thrust on caudal fin increases. The power consumed by the trunk show no significant change as Re increases and the caudal fin power consumption enlarges. The growth rates of these hydrodynamic coefficients for all cases decrease with increasing Re. It is indicated that

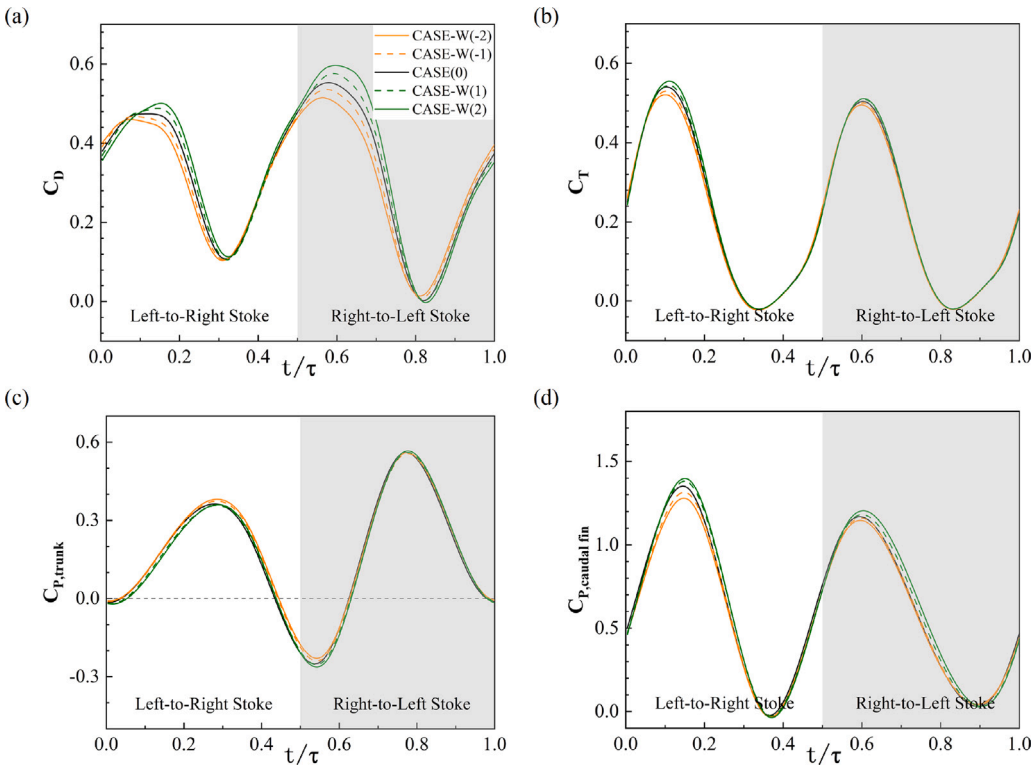

Fig. 15. Time histories of: (a) drag coefficients of TK, (b) thrust coefficients of CF, power consumption coefficients of (c) TK and (d) CF of varying width during one whole undulatory cycle.

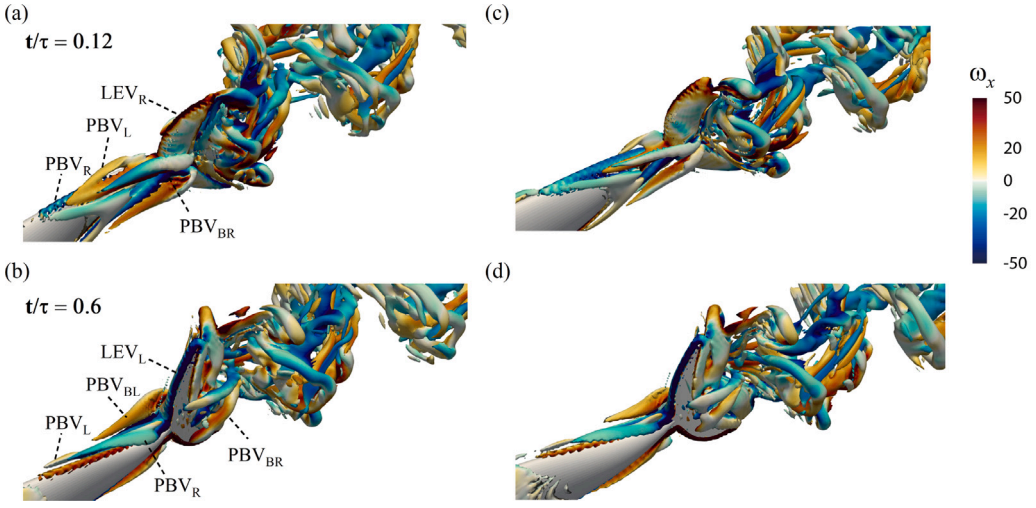

Fig. 16. Instantaneous three-dimensional wake structures of tuna models with different posterior body height: (a)(b) CASE-W(−2), and (c)(d) CASE-W(2) at (a)(c) $t/\tau = 0.12$, (b)(d) $t/\tau = 0.6$. The coherent structures are visualized by the iso-surface $Q = 50$ of the Q-criterion and colored by x−component of vorticity ω_x.

the inertia force gradually dominates after *Re* reaches a certain value. Furthermore, the effects due to posterior body morphology still work with changing *Re*.

Fig. 20(a) shows that the trunk drag only enlarges for a limited period during the peaks of varying height as *Re* increases, while Fig. 20(b) presents that the drag enlarges for most time in the undulatory cycle with increasing width. Furthermore, in Fig. 20(c), we find the caudal fin thrust in CASE-H(2) is clearly higher than that in CASE-H(−2) at different *Re*. However, as the width is increased, the thrust mainly enlarges around peaks in the C_T curves depicted in Fig. 20(d). These findings underscores that *Re* is important to the hydrodynamic performance of thunniform swimming and the effects due to posterior body morphology is almost universal at different *Re*.

Fig. 21 shows the 3D wake structures and contours of the spanwise vorticity distributions on the $x-y$ plane for CASE-H(−2) at varying *Re*. The wake mainly made up of vortices generated from caudal fin resembles a reversed *Kármán* vortex street and these wake patterns reveal strong similarities at different *Re*. The critical flow structures have no major difference within a wide range of *Re*, showing that the simulated wake structures are in good agreement with the experiments (Zhong et al., 2019). In addition, we observe that the thickness of viscous regions around the anterior body shrinks and the overall width of the wake become greater as *Re* increases. Fig. 21(a) shows double row wake consisting of laterally dislocated vortex loops at $Re = 1600$ and wake structure becomes significantly more complex with increasing *Re*. The double row wake pattern is no longer composed of two simple

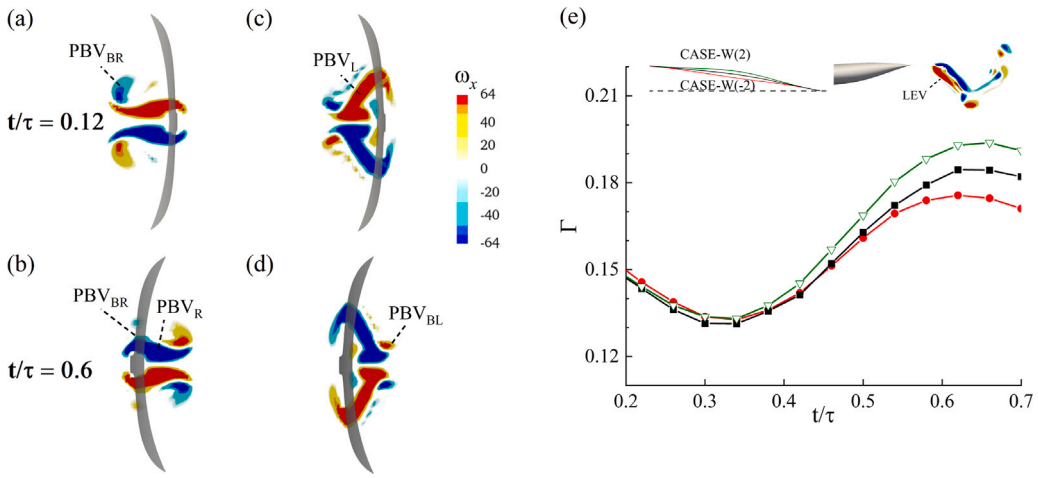

Fig. 17. Contour of normalized ω_x on a vertical plane located at $0.80L$ cutting through the flow field of (a)(b) CASE-W(−2), (c)(d) CASE-W(2). (e) Circulation (Γ) of vorticity ω_z from the LEV attached to the leftside of CF surface on the slice, whose position is through the top CF leading edge.

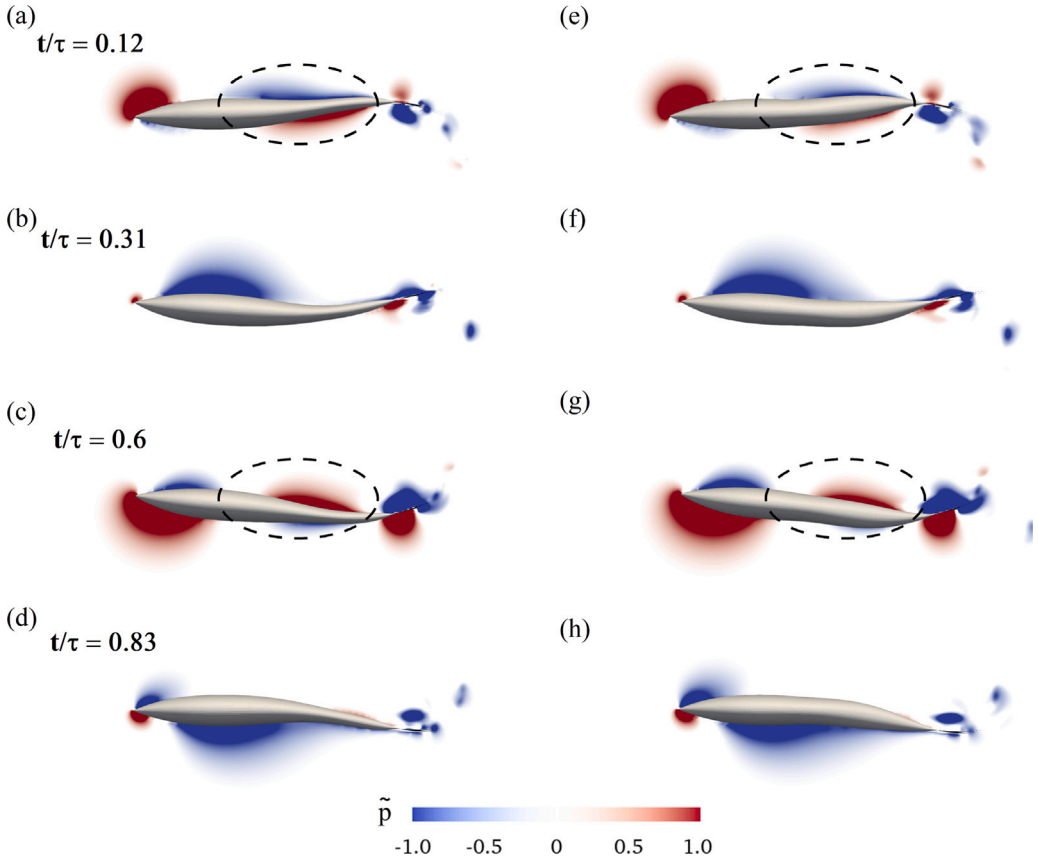

Fig. 18. Contours of pressure coefficient $\tilde{p}$ in the mid-span of (a)–(d) CASE-W(−2), and (e)–(h) CASE-W(2) cutting through the flow field at different time step. These two colors indicate pushing (red) and suction (blue) forces acting on the body surface, respectively.

vortex loops rows but consists of complex and highly 3D coherent structures at high Re. As shown in Fig. 21(d)–(f), the wake vortices are qualitatively similar at different Re and the downstream vortices diminish faster when Re is small. Variations of cycle-averaged streamwise velocity with increasing Re in the cross-stream (y) direction at two different positions behind the caudal fin are plotted in Fig. 21(g)(h), respectively. It can be seen that the undulation for tuna model at $Re = 1600$ (blue line) is dragged by the viscous fluid with lower velocity than ambient streamwise velocity($1.6L/s$). As Re becomes higher, the thrust manifested by the streamwise velocity has been enhanced. This suggests forward thrust produced by caudal fin starts to overcome the drag acting on the trunk as Re increases.

3.4. Effect of the Strouhal number

The effect of St is further examined in the range of 0.25–0.75 at fixed $Re = 6400$. St is only adjusted by changing the undulatory frequency (f) while the maximum amplitude (A_m) is kept constant. Fig. 22(a) shows the trunk drag reduction becomes more significant due to decreasing width as St increases while the drag has little difference

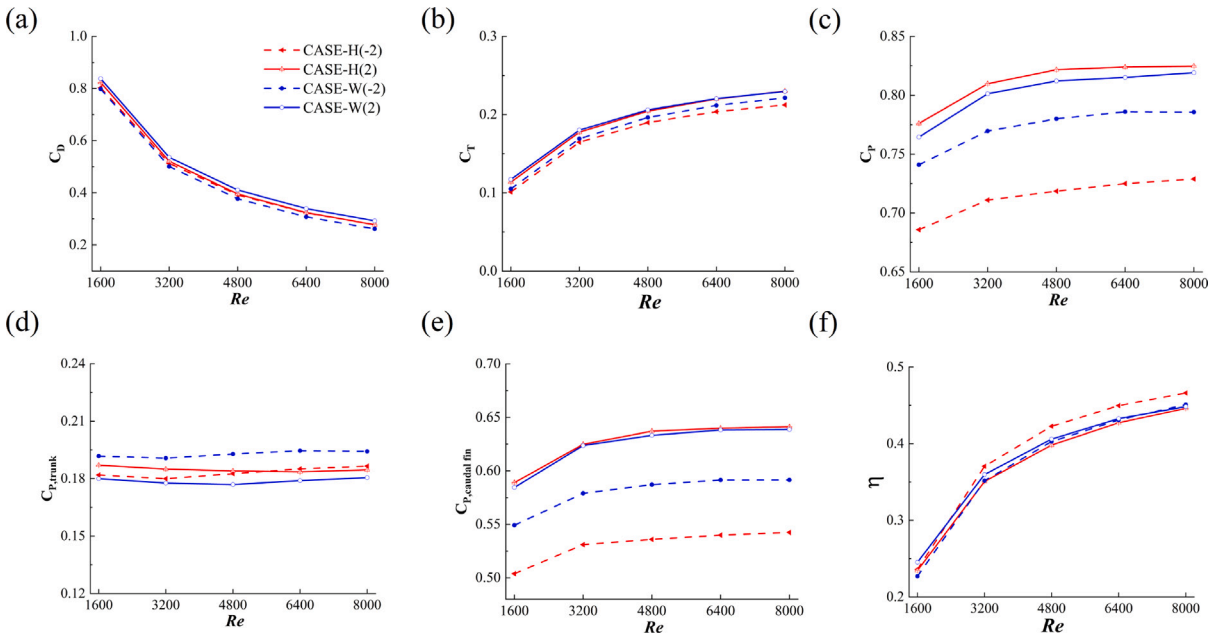

Fig. 19. Cycle-averaged coefficients for the models of different posterior body shapes with respect to *Re*: (a) drag coefficients of TK, (b) thrust coefficients of CF, power consumption coefficients of (c) the whole model, (d) TK and (e) CF, and (f) the caudal fin efficiency.

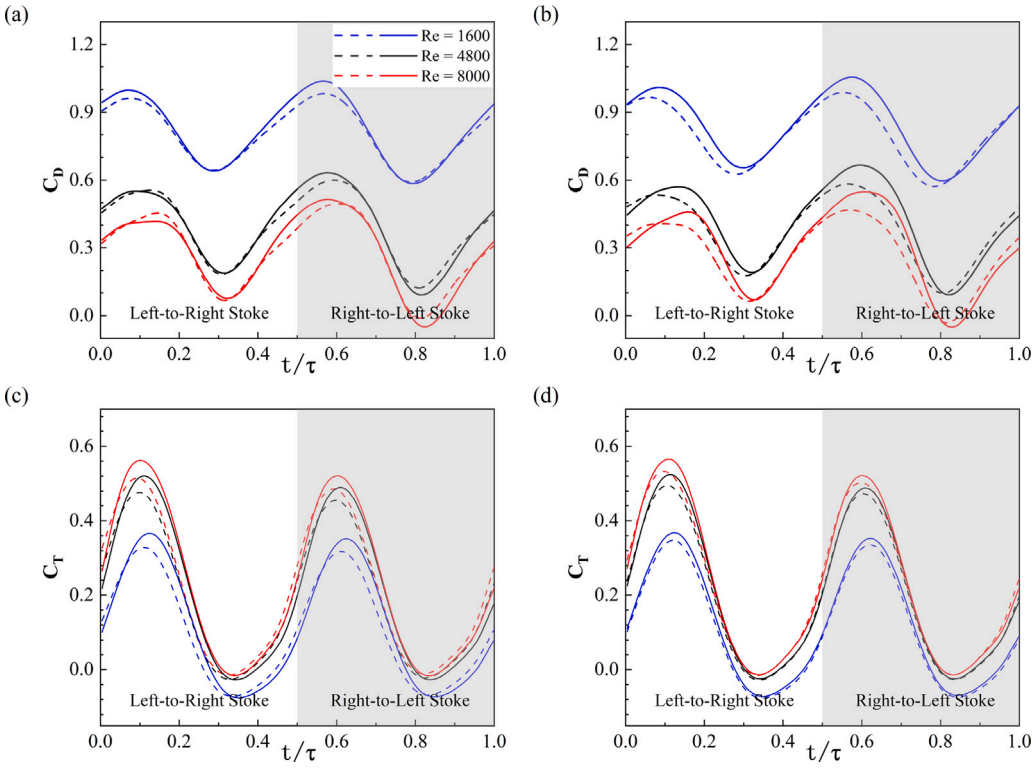

Fig. 20. Time histories of drag coefficients of (a) varying heights and (b) varying widths for different *Re*. Time histories of caudal fin thrust coefficients of (c) varying heights and (d) varying widths for different *Re*. The dashed lines represent (a,c) CASE-H(−2) and (b,d) CASE-W(−2), respectively. The solid lines represent (a,c) CASE-H(2) and (b,d) CASE-W(2), respectively.

with varying height. On the other hand, as shown in Fig. 22(b), the caudal fin thrust is substantially increased with increasing *St*. In addition, the caudal fin thrust enhancement becomes more obvious due to posterior body morphology. Moreover, this enhancement is magnified more by height modification than width change. Power consumption by trunk and caudal fin enlarges greatly with increasing *St* as depicted in Fig. 22(d)(e). The trunk power consumption predicted with different posterior body shapes are nearly identical at the same *St*, suggesting that posterior body morphology has no noticeable influence on trunk power consumption. However, when *St* becomes higher, the increase of caudal fin power consumption due to posterior body morphology is magnified, especially with increasing height. We also find the efficiency reaches maximum at $St = 0.375$ for different posterior body shapes, which agrees with previous studies (Lucas et al., 2014; Saadat et al.,

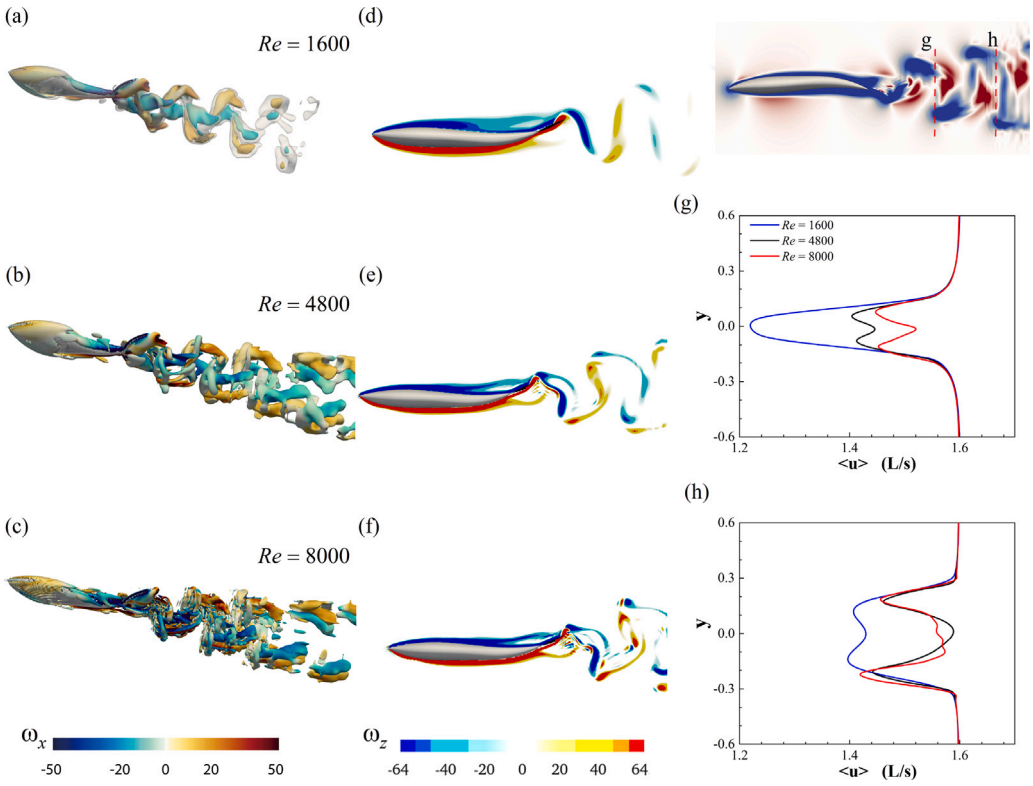

Fig. 21. (a)–(c) Instantaneous three-dimensional wake structures of CASE-H(−2) at $t/\tau = 0.12$; The coherent structures are visualized by the iso-surface $Q = 50$ of the Q-criterion and colored by x−component of vorticity ω_x. (d)–(f) contours of the normalized spanwise vorticity ω_z on the x-y plane for various Re; (g) and (h) variations of cycle-averaged streamwise velocity ($\langle u \rangle$) in the cross-stream direction for two slices, whose positions are shown by the red lines on top of these figures.

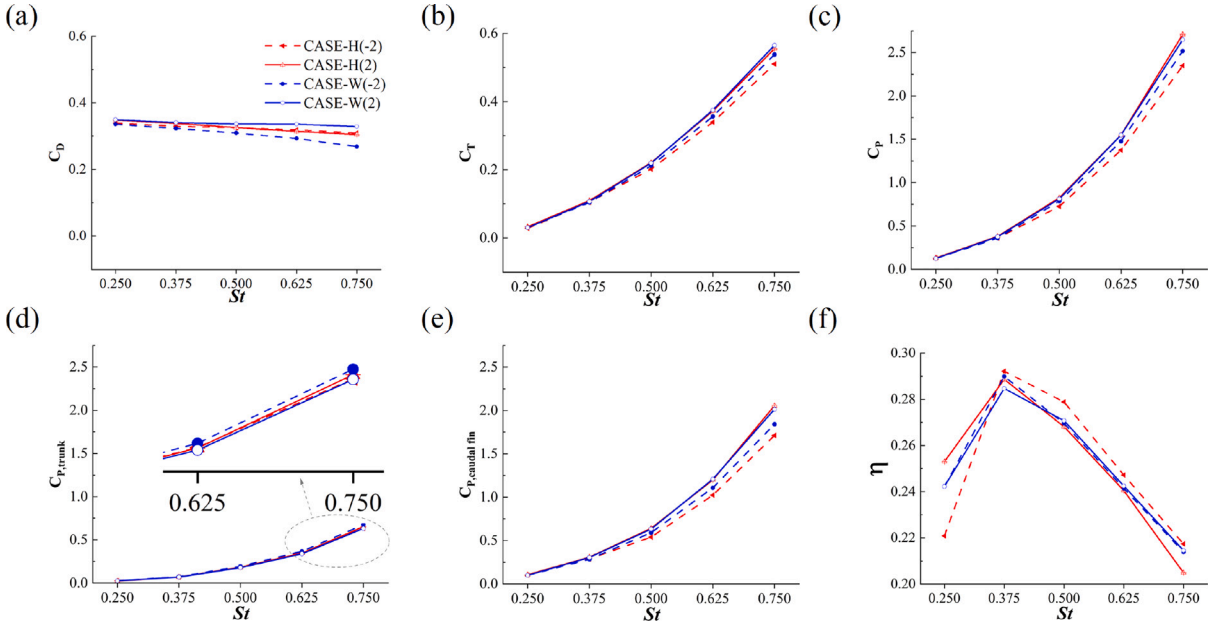

Fig. 22. Cycle-averaged hydrodynamic coefficients for the models of different posterior body shapes with respect to St: (a) drag coefficients of TK, (b) thrust coefficients of CF, power consumption coefficients of (c) the whole model, (d) TK and (e) CF, and (f) the caudal fin efficiency.

2017) that efficient locomotion for swimmers in nature occurs when St in the range of 0.2–0.4 and A/L in the tight range of 0.1–0.3.

For these cases with different posterior body shapes, time histories of trunk drag coefficients almost overlap each other at the same St. So we take CASE-H(−2) with varying St shown in Fig. 23(a) as an example, which presents peak values are enlarged and valleys are decreased as St increases. Fig. 23(b), the comparison of caudal fin thrust between CASE-H(−2) and CASE-H(2), shows the peaks in caudal fin thrust are enlarged remarkably for height change as St increases. However, as shown in Fig. 23(c), the thrust enhancement due to width increase is not obvious at different St.

Fig. 24(a)–(e) presents three-dimensional vortical structures and Fig. 24(f)–(j) shows contours of spanwise vorticity distributions on the $x - y$ plane for CASE-H(−2) with varying St. The wake structure is

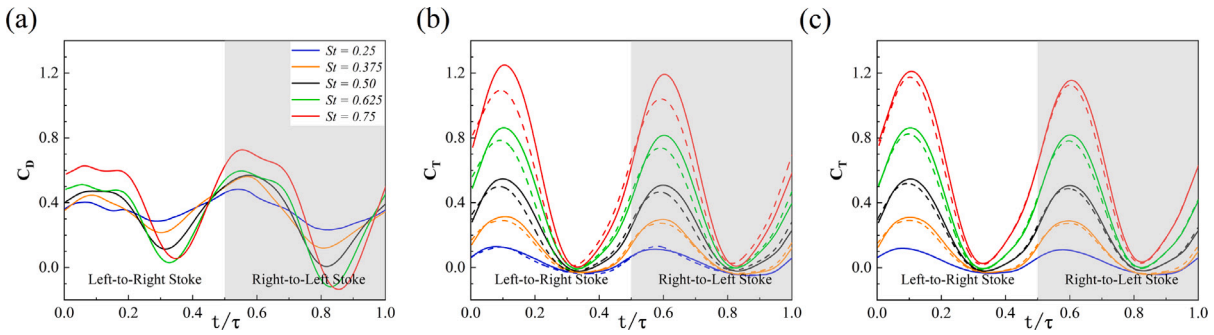

Fig. 23. (a) Time histories of drag coefficients of CASE-W(−2) for various St. Time histories of caudal fin thrust coefficients of (b) varying height and (c) varying width for various St. The solid lines represent (b) CASE-H(2) and (c) CASE-W(2), respectively. The dashed lines represent (b) CASE-H(−2) and (c) CASE-W(−2), respectively.

expected to primarily depend on the St. At low St, in Fig. 24(a) (b), a wake mainly consists of a single row of vortices. At $St = 0.375$, the single row wake is shortened in streamwise direction and the trend towards splitting double row wake appears. As St continues to increase, a double row of vortices is observed in Fig. 24(c)–(e), and the double row wake becomes more evident. With increasing St, vortices are advected away from the centerline, causing them to spread in the lateral direction. And the wake diverged laterally is efficiently enhanced. Body undulations at higher St generally imply faster lateral undulations, which results in higher lateral power loss, more power consumption and lower efficiency. What is more, the vortex wake mainly composes of vortices shed from caudal fin and resembles a *Kármán* street that manifests drag at $St = 0.25$ in Fig. 24(f). As shown in Fig. 24(g)–(j), with increasing St, the wake resembles a reversed *Kármán* vortex street, which represents thrust production.

Plots of cycle-averaged thrust distributions in Fig. 25 indicate that, at different St, most of the thrust is generated in the leading edge region of the caudal fin. With increasing St, the magnitude of cycle-averaged thrust produced by the caudal fin increases greatly, which implies that LEV is responsible for caudal fin thrust generation.

4. Conclusion

Previous studies mainly focused on the hydrodynamic performance affected by specialized features of thunniform swimmers, e.g., finlets, crescent caudal fin and lateral caudal keels on the peduncle, while less researches on trunk morphology have been done. The large amplitude of undulation for thunniform swimmers is primarily restricted to one-half or one-third posterior part of the body, which is crucial to determine their high cruising speed. In the present paper, for the designated undulation characteristics of thunniform swimmers, we investigate how the posterior body morphology adjusts propulsion performance.

By analyzing hydrodynamics and wake topology, it is demonstrated that even a small range of posterior body morphological change can enhance the swimming performance. Modifications in height of posterior body have a greater impact on caudal fin thrust than modifications in width, which improves relative C_T from 95.8% to 103.5% with respect to the original case (CASE(0)). Such enhancement is attributed to the constructive interaction between PBV_s and LEV_s, which distinctively intensifies the LEV_s. Reducing posterior body width diminishes the trunk drag from 105.2% to 95.2% with respect to the original case, while height change slightly affects the trunk drag. Also, the interaction between PBV_R and PBV_L near the posterior region evidently weakens, which enlarges the difference of PBV_s attached to the left and right side of trunk. The pressure difference between the two sides of posterior body resulting from PBV_s helps with the alleviation of the trunk drag, which is more evident with decreasing width. It is interesting that the caudal fin efficiency shrinks with the increase of height whereas improves slightly with the increase of width.

For different posterior body shapes, the effects of various Re and St are systematically investigated. As Re increases, the trunk drag decreases significantly and the caudal fin thrust enhances. After reaching a certain value of Re, the inertia force gradually dominates, which slows down the force change. For various posterior body shapes, most hydrodynamic properties, e.g., C_D, C_T and C_P show consistent trend at different Re, which suggests the effects due to posterior body morphology are almost universal. The wake structure (double row $vs.$ single row) mainly depends on St, which alters the swimming performance substantially. As St increases, the caudal fin thrust greatly enhances whereas the trunk drag slightly decreases. With increasing St, the enhancement of thrust due to increasing height outweighs that of increasing width, while drag reduction due to width modification outweighs that of height modification. It is demonstrated that St increase leads to more constructive interaction of PBV_s and LEV_s, and the constructive interaction is magnified by varying height as St increases. In addition, the efficiency reaches maximum (about 0.3) for all the cases when $St = 0.375$, lying in the range of 0.2–0.4 for most swimmers in nature.

This paper confirms the propulsion mechanism of posterior body morphology for thunniform swimmers, which lays the foundation for design of high-performance artificial swimming devices.

CRediT authorship contribution statement

Shun Huang: Software, Validation, Data curation, Formal analysis, Writing – original draft. **Dilong Guo:** Conceptualization, Data curation, Writing – review & editing. **Yiwei Wang:** Methodology. **Guowei Yang:** Conceptualization, Resources. **Bo Yin:** Conceptualization, Methodology, Resources, Writing – review & editing.

Declaration of competing interest

The authors declare that they have no known competing financial interests or personal relationships that could have appeared to influence the work reported in this paper.

Data availability

Data will be made available on request.

Acknowledgments

This work was supported by the Strategic Priority Research Program of the Chinese Academy of Sciences (class A) (Grant No. XDA22040203).

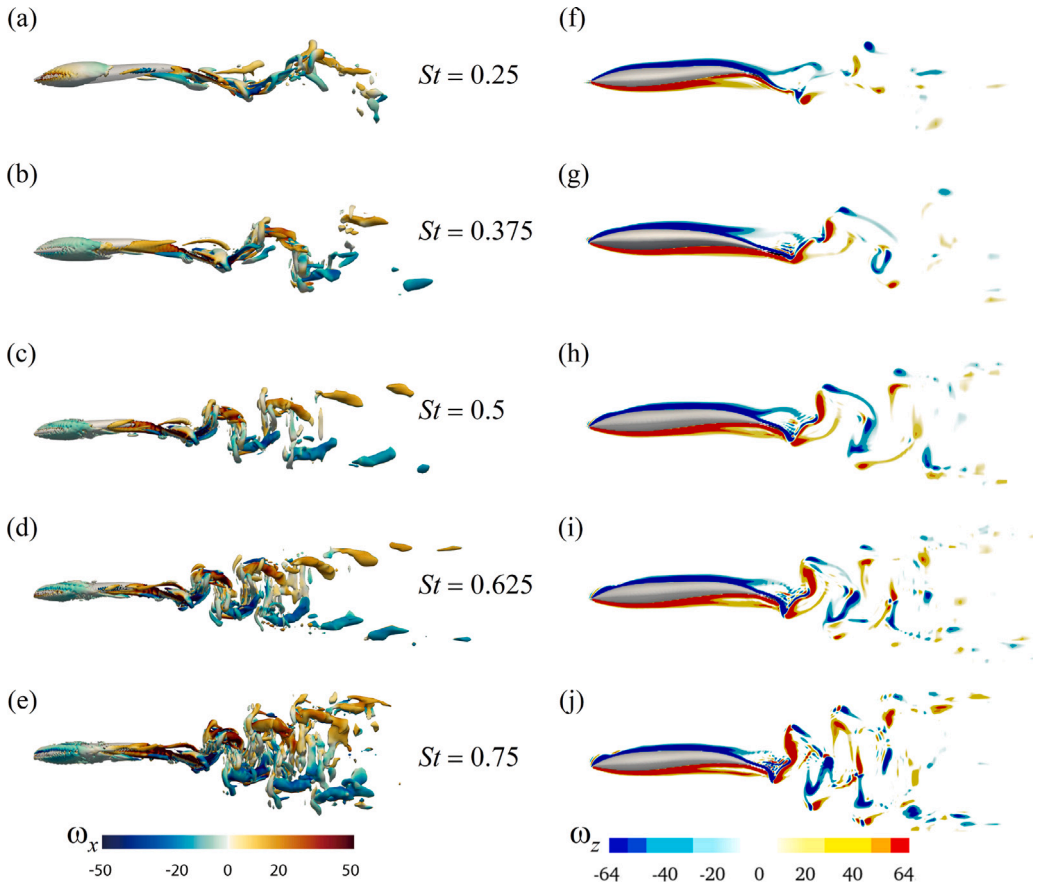

Fig. 24. (a)–(e) Instantaneous three-dimensional wake structures of CASE-H(−2) at $t/\tau = 0.12$; The coherent structures are visualized by the iso-surface $Q = 50$ of the Q-criterion and colored by x−component of vorticity ω_x. (f)–(j) contours of the normalized spanwise vorticity ω_z on the x-y plane for various St;.

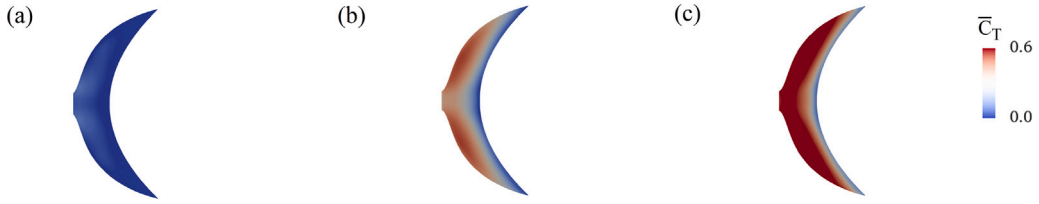

Fig. 25. Distribution of the cycle-averaged thrust coefficients ($\bar{C}_T$) on the caudal fin at $t/\tau = 0.6$ for CASE-H(2) at (a) $St = 0.25$; (b) $St = 0.375$; (c) $St = 0.625$.

References

Anderson, J.M., Chhabra, N.K., 2002. Maneuvering and stability performance of a robotic tuna. Integr. Comp. Biol. 42 (1), 118–126.

Arreola, V.I., Westneat, M.W., 1996. Mechanics of propulsion by multiple fins: kinematics of aquatic locomotion in the burrfish (Chilomycterus schoepfi). Proc. R. Soc. B 263 (1377), 1689–1696.

Barrett, D., Triantafyllou, M., Yue, D., Grosenbaugh, M., Wolfgang, M., 1999. Drag reduction in fish-like locomotion. J. Fluid Mech. 392, 183–212.

Borazjani, I., Sotiropoulos, F., 2008. Numerical investigation of the hydrodynamics of carangiform swimming in the transitional and inertial flow regimes. J. Exp. Biol. 211 (10), 1541–1558.

Borazjani, I., Sotiropoulos, F., 2009. Numerical investigation of the hydrodynamics of anguilliform swimming in the transitional and inertial flow regimes. J. Exp. Biol. 212 (4), 576–592.

Borazjani, I., Sotiropoulos, F., 2010. On the role of form and kinematics on the hydrodynamics of self-propelled body/caudal fin swimming. J. Exp. Biol. 213 (1), 89–107.

Bozkurttas, M., Mittal, R., Dong, H., Lauder, G., Madden, P., 2009. Low-dimensional models and performance scaling of a highly deformable fish pectoral fin. J. Fluid Mech. 631, 311–342.

Chang, X., Zhang, L., He, X., 2012. Numerical study of the thunniform mode of fish swimming with different Reynolds number and caudal fin shape. Comput. & Fluids 68, 54–70.

Clift, R., Grace, J.R., Weber, M.E., 2005. Bubbles, drops, and particles.

Collette, B., Nauen, C., 1983. An annotated and illustrated catalogue of Tunas, Mackerels, Bonitos and related species known to date. FAO Species Catalogue. Vol. 2. Scombrids of the world. FAO Fish. Synop 125 (2).

De, A.K., Sarkar, S., 2021. Dependence of wake structure on pitching frequency behind a thin panel at. J. Fluid Mech. 924.

Dewar, H., Graham, J., 1994. Studies of tropical tuna swimming performance in a large water tunnel-kinematics. J. Exp. Biol. 192 (1), 45–59.

Donley, J.M., Dickson, K.A., 2000. Swimming kinematics of juvenile kawakawa tuna (Euthynnus affinis) and chub mackerel (Scomber japonicus). J. Exp. Biol. 203 (20), 3103–3116.

Donley, J.M., Sepulveda, C.A., Konstantinidis, P., Gemballa, S., Shadwick, R.E., 2004. Convergent evolution in mechanical design of lamnid sharks and tunas. Nature 429 (6987), 61–65.

Drucker, E.G., Lauder, G.V., 2002. Experimental hydrodynamics of fish locomotion: functional insights from wake visualization. Integr. Comp. Biol. 42 (2), 243–257.

Fish, F.E., 1998. Comparative kinematics and hydrodynamics of odontocete cetaceans: morphological and ecological correlates with swimming performance. J. Exp. Biol. 201 (20), 2867–2877.

Han, P., Lauder, G.V., Dong, H., 2020. Hydrodynamics of median-fin interactions in fish-like locomotion: Effects of fin shape and movement. Phys. Fluids 32 (1), 011902.
Hunt, J., Wray, A., Moin, P., 1988. Eddies, Streams, and Convergence Zones in Turbulent Flows. Center for Turbulence Research Report CTR-S88, pp. 193–208.
Khalid, M.S.U., Wang, J., Akhtar, I., Dong, H., Liu, M., Hemmati, A., 2021. Larger wavelengths suit hydrodynamics of carangiform swimmers. Phys. Rev. Fluids 6 (7), 073101.
Lauder, G.V., 2015. Fish locomotion: recent advances and new directions. Annu. Rev. Mar. Sci. 7 (1), 521–545.
Li, N., Liu, H., Su, Y., 2017. Numerical study on the hydrodynamics of thunniform bio-inspired swimming under self-propulsion. PLoS One 12 (3), e0174740.
Li, G.-j., Luodin, Z., Lu, X.-y., 2012. Numerical studies on locomotion perfromance of fish-like tail fins. J. Hydrodynamics, Ser. B 24 (4), 488–495.
Lighthill, M., 1969. Hydromechanics of aquatic animal propulsion. Annu. Rev. Fluid Mech. 1 (1), 413–446.
Lindsey, C., 1978. Form, function and locomotory habits in fish. In: Locomotion.
Liu, G., Ren, Y., Dong, H., Akanyeti, O., Liao, J.C., Lauder, G.V., 2017. Computational analysis of vortex dynamics and performance enhancement due to body–fin and fin–fin interactions in fish-like locomotion. J. Fluid Mech. 829, 65–88.
Lucas, K.N., Johnson, N., Beaulieu, W.T., Cathcart, E., Tirrell, G., Colin, S.P., Gemmell, B.J., Dabiri, J.O., Costello, J.H., 2014. Bending rules for animal propulsion. Nature Commun. 5 (1), 1–7.
Luo, H., Dai, H., de Sousa, P.J.F., Yin, B., 2012. On the numerical oscillation of the direct-forcing immersed-boundary method for moving boundaries. Comput. & Fluids 56, 61–76.
Luo, H., Yin, B., Dai, H., Doyle, J., 2010. A 3D computational study of the flow-structure interaction in flapping flight. In: 48th AIAA Aerospace Sciences Meeting Including the New Horizons Forum and Aerospace Exposition. p. 556.
Magnuson, J.J., 1970. Hydrostatic equilibrium of Euthynnus affinis, a pelagic teleost without a gas bladder. Copeia 56–85.
Magnuson, J.J., 1978. Locomotion by scombrid fishes: Hydromechanics, morphology, and behaviour. Fish Physiol. 240–313.
Marella, S., Krishnan, S., Liu, H., Udaykumar, H., 2005. Sharp interface Cartesian grid method I: an easily implemented technique for 3D moving boundary computations. J. Comput. Phys. 210 (1), 1–31.
Mather, F.J., 1962. Transatlantic migration of two large bluefin tuna. ICES J. Mar. Sci. 27 (3), 325–327.
Mittal, R., Dong, H., Bozkurttas, M., Najjar, F., Vargas, A., Von Loebbecke, A., 2008. A versatile sharp interface immersed boundary method for incompressible flows with complex boundaries. J. Comput. Phys. 227 (10), 4825–4852.
Nauen, J.C., Lauder, G.V., 2002. Hydrodynamics of caudal fin locomotion by chub mackerel, Scomber japonicus (Scombridae). J. Exp. Biol. 205 (12), 1709–1724.
Saadat, M., Fish, F.E., Domel, A., Di Santo, V., Lauder, G., Haj-Hariri, H., 2017. On the rules for aquatic locomotion. Phys. Rev. Fluids 2 (8), 083102.
Sfakiotakis, M., Lane, D.M., Davies, J.B.C., 1999. Review of fish swimming modes for aquatic locomotion. IEEE J. Ocean. Eng. 24 (2), 237–252.
Shadwick, R.E., 2005. How Tunas and Lamnid Sharks Swim: An Evolutionary Convergence: These fishes diverged millions of years ago, but selection presures have brought them very similar biomechanical schemes for movement. Am. Sci. 93 (6), 524–531.
Shadwick, R.E., Syme, D.A., 2008. Thunniform swimming: muscle dynamics and mechanical power production of aerobic fibres in yellowfin tuna (Thunnus albacares). J. Exp. Biol. 211 (10), 1603–1611.
Smits, A.J., 2019. Undulatory and oscillatory swimming. J. Fluid Mech. 874.
Song, J., Zhong, Y., Du, R., Yin, L., Ding, Y., 2021. Tail shapes lead to different propulsive mechanisms in the body/caudal fin undulation of fish. Proc. Inst. Mech. Eng. C 235 (2), 351–364.
Triantafyllou, M.S., Triantafyllou, G.S., 1995. An efficient swimming machine. Sci. Am. 272 (3), 64–70.
Triantafyllou, M.S., Triantafyllou, G., Yue, D., 2000. Hydrodynamics of fishlike swimming. Annu. Rev. Fluid Mech. 32 (1), 33–53.
Van Rees, W.M., Gazzola, M., Koumoutsakos, P., 2013. Optimal shapes for anguilliform swimmers at intermediate Reynolds numbers. J. Fluid Mech. 722.
Van Rees, W.M., Gazzola, M., Koumoutsakos, P., 2015. Optimal morphokinematics for undulatory swimmers at intermediate Reynolds numbers. J. Fluid Mech. 775, 178–188.
Videler, J.J., 1993. Fish Swimming, Vol. 10. Springer Science & Business Media.
Wang, J., Tran, H., Christino, M., White, C., Zhu, J., Lauder, G., Bart-Smith, H., Dong, H., 2019. Hydrodynamics and flow characterization of tuna-inspired propulsion in forward swimming. In: Fluids Engineering Division Summer Meeting, Vol. 59025. American Society of Mechanical Engineers, V001T01A025.
Webb, P.W., 1994. The biology of fish swimming. Mech. Physiol. Animal Swim. 4562.
White, C.H., Lauder, G.V., Bart-Smith, H., 2021. Tunabot flex: a tuna-inspired robot with body flexibility improves high-performance swimming. Bioinspiration Biomim. 16 (2), 026019.
Xia, D., Chen, W., Liu, J., Wu, Z., Cao, Y., 2015. The three-dimensional hydrodynamics of thunniform swimming under self-propulsion. Ocean Eng. 110, 1–14.
Yin, B., Yang, G., Prapamonthon, P., 2019. Finite obstacle effect on the aerodynamic performance of a hovering wing. Phys. Fluids 31 (10), 101902.
Zhang, J.-D., Huang, W.-X., 2022. Numerical model and hydrodynamic performance of tuna finlets. Theor. Appl. Mech. Lett. 12 (1), 100322.
Zhang, J.-D., Sung, H.J., Huang, W.-X., 2020. Specialization of tuna: A numerical study on the function of caudal keels. Phys. Fluids 32 (11), 111902.
Zhong, Q., Dong, H., Quinn, D.B., 2019. How dorsal fin sharpness affects swimming speed and economy. J. Fluid Mech. 878, 370–385.
Zhu, J., White, C., Wainwright, D.K., Di Santo, V., Lauder, G.V., Bart-Smith, H., 2019. Tuna robotics: A high-frequency experimental platform exploring the performance space of swimming fishes. Science Robotics 4 (34), eaax4615.
Zhu, Q., Wolfgang, M., Yue, D., Triantafyllou, M., 2002. Three-dimensional flow structures and vorticity control in fish-like swimming. J. Fluid Mech. 468, 1–28.